ADVANCED NANOBIOMED RESEARCH
www.advnanobiomedres.com

Tri-Modal Anticancer Strategies with Doxorubicin-Loaded Iron Oxide Nanoparticles Integrating Chemo and Magneto-Photothermal Therapeutic Effects

*Rosalía López-Méndez, Nuria Lafuente-Gómez, Eva Céspedes, Mónica Dhanjani, Marina París-Ogáyar, Francisco José Terán, Aida Serrano, Julio Camarero, Gorka Salas, Claire Wilhelm, Álvaro Somoza, and Ana Espinosa**

In this study, the potential of maghemite (γ-Fe_2O_3) nanoparticles (MNPs) functionalized with doxorubicin (DOX) is explored for chemo-magneto-photothermal therapy in cancer treatment. MNPs are functionalized through electrostatic interactions or disulfide bonds, achieving high drug-loading efficiencies. The trimodal approach combines magnetic hyperthermia (MHT), photothermal therapy (PTT) and local chemotherapy, utilizing low and clinically relevant doses. Thermal treatments induced controlled temperature increases, triggering pH-sensitive DOX release in the acidic environments typical of tumors. Efficient uptake of DOX-loaded MNPs is observed, and their structural integrity is confirmed using advanced synchrotron spectroscopic techniques. Cytotoxicity assays show that MHT and PTT together enhanced therapeutic efficacy compared to free DOX, while minimizing toxicity to healthy cells. This study demonstrates that combining thermal therapies with controlled drug release provides a promising strategy for improving cancer treatment outcomes. The findings highlight the potential clinical application of multifunctional nanoparticle systems for targeted, low-toxicity cancer therapies, advancing the path toward more effective and accessible treatments.

1. Introduction

Iron oxide nanoparticles (IONPs) have gained recognition as excellent candidates for biomedical applications due to their combined functions, biocompatibility and biodegradability, with unique iron-derived mechanisms governing their storage and degradation processes.[1–3] In cancer nanomedicine, IONPs offer significant advantages, particularly as magnetic particles that can be guided toward tumor sites using an external magnetic field[4] and can serve as contrast agents in imaging.[5,6] Additionally, IONPs can effectively function as nanocarriers in stimulus-triggered drug delivery treatments.[7] Furthermore, as single-domain magnetic nanoparticles (MNPs), they generate heat through relaxation loss[8–11] upon exposure to an alternating magnetic field (AMF), and they have

R. López-Méndez, N. Lafuente-Gómez, M. Dhanjani, M. París-Ogáyar, F. José Terán, J. Camarero, G. Salas, Á. Somoza
IMDEA Nanociencia
c/ Faraday, 9, 28049 Madrid, Spain

E. Céspedes, A. Espinosa
Instituto de Ciencia de Materiales de Madrid
ICMM-CSIC
28049 Madrid, Spain
E-mail: ana.espinosa@csic.es

M. París-Ogáyar, A. Serrano
Departamento de Electrocerámica
Instituto de Cerámica y Vidrio
ICV-CSIC
Kelsen 5, 28049 Madrid, Spain

The ORCID identification number(s) for the author(s) of this article can be found under https://doi.org/10.1002/anbr.202500098.

DOI: 10.1002/anbr.202500098

M. París-Ogáyar
Nanomaterials for Bioimaging Group (nanoBIG)
Departamento de Física de Materiales–Facultad de Ciencias
Universidad Autónoma de Madrid
c/ Francisco Tomás y Valiente, 7, 28049 Madrid, Spain

F. José Terán, G. Salas, A. Espinosa
Unidad asociada de Nanomateriales Avanzados
IMDEA Nanociencia – Instituto de Ciencia de Materiales de Madrid (ICMM-CSIC)
28049 Madrid, Spain

J. Camarero
Departamento de Física de la Materia Condensada and Instituto 'Nicolás Cabrera'
Universidad Autónoma de Madrid
28049 Madrid, Spain

G. Salas, Á. Somoza
Unidad Asociada de Nanobiotecnología (CNB-CSIC e IMDEA Nanociencia)
28049 Madrid, Spain

C. Wilhelm
Laboratoire Physico Chimie Curie, PCC, CNRS UMR168, Institut Curie
Sorbonne University
PSL University
75005 Paris, France

also been extensively used in magnetic hyperthermia treatment (MHT).[12,13]

Recently, they have also been proposed as promising candidates for photothermal therapy (PTT),[14–21] despite their relatively low molar extinction coefficient, compared with metallic NPs.[19,22–27] In PTT, radiation energy causes a temporary transition of electrons from the valence band to the conduction band, and the energy is converted to heat as the electrons return to the valence band.[28] Typically, near-infrared (NIR) radiation is used, operating within the first and second biological windows (650–900 and 1000–1400 nm, respectively). These wavelength ranges allow for minimal light absorption and scattering by tissues, resulting in greater penetration depth and reduced tissue self-heating, which minimizes damage to adjacent healthy tissues.[10,29]

Therefore, IONPs can act as hyperthermia agents when exposed to an AMF or NIR light. Hyperthermia is a treatment that involves raising body temperature above normal levels, where targeted tumor sites reach temperatures within the range of 41–48 °C.[30] At these temperatures, cellular processes are triggered that promote the activation of cell death mechanisms, such as protein inactivation, inhibition of DNA synthesis and repair, and alterations in signal transduction pathways.[10] The fact that IONPs can induce hyperthermia through two physically orthogonal mechanisms (PTT and MHT) makes them truly unique in the field of thermal therapies. Indeed, heating efficiency can be synergistically enhanced through a dual approach combining MHT and PTT, referred to as magneto-photothermia,[4,14,31–33] which can be achieved using only iron oxide-based NPs.[14] This approach allows for the reduction of nanoparticle concentration and laser power density, resulting in a cumulative or even synergistic increase in the specific absorption rate (SAR) for IONPs in cells.[34,35] This dual heating can lead to complete tumor ablation *in vivo*.[14]

Additionally, IONPs have also been explored as drug delivery systems due to their ability to carry anticancer drugs with high loading capacity,[36,37] releasing therapeutic agents in a controlled manner through the heat generated during AMF or light exposure.[12,38,39]

Effective multimodal treatments based on IONPs have been investigated, integrating chemotherapy with MHT,[13,37,39–44] as well as PTT.[38,45,46] Besides, several studies have exploited the magnetic properties of IONPs to guide them to targeted regions using external magnetic fields, thereby enhancing the localized delivery of therapeutic agents, followed by combination treatments, such as chemo-photothermia.[4,46–48] While a few studies have suggested the potential for future trimodal treatments,[49,50] only one study has reported an *in vivo* application that combines MHT, PTT and chemotherapy.[51] However, in all reported cases of trimodal treatments, the PTT illumination doses exceeded 1 W cm^{-2}, and the MHT parameters surpassed clinically safe limits.

This study introduces a trimodal chemo-magneto-photothermal cancer therapy based on MNPs. These nanoparticles, coated with meso-2,3-dimercaptosuccinic acid (DMSA), are loaded with the anticancer drug doxorubicin (DOX), to enable localized drug release at the tumor site. The drug release is triggered by heat generated during magneto-photothermia, achieved through the simultaneous application of an AMF and a NIR laser (808 nm) at safe doses (103 kHz, 20 mT and 0.23 W cm^{-2}, respectively). This multimodal approach significantly enhances tumor cell death by harnessing the synergistic effects of the three therapeutic modalities. Overall, this study demonstrates a trimodal treatment using DOX-loaded MNPs as an effective localized therapy with the potential to minimize side effects.

2. Results

2.1. Synthesis and Elemental Characterization of MNPs

MNPs were successfully prepared through a coprecipitation method,[52,53] followed by an oxidative acid treatment aimed at obtaining γ-Fe_2O_3 (and avoid further issues of iron oxidation under physiological conditions),[54,55] which yielded particles with a spherical shape and a diameter mean size of 14 ± 4 nm (**Figure 1**A,B and S1, Supporting Information). They were coated with DMSA to improve their stability. Structural analysis of the obtained samples by X-ray diffraction (XRD) revealed the formation of a cubic spinel structure (Figure 1C), which may be indexed as either magnetite (Fe_3O_4) or maghemite (γ-Fe_2O_3) (JCPDS card nos. 39-1346, 19-629 and 00-015-0615). However, confirming the maghemite phase by XRD is challenging because magnetite and maghemite possess a similar structure and nearly identical lattice parameters.[56] Magnetite exhibits cubic symmetry with a spinel structure, while maghemite has an inverse spinel structure with some cation deficiency. Specifically, one out of every six octahedral sites in magnetite is vacant in the maghemite structure.[57] Therefore, the phase of MNP was further confirmed using Raman spectroscopy. According to the literature, magnetite shows the most characteristic bands at 670 and 535 cm^{-1}, corresponding to the A_{1g} and T_{2g} transitions,[58] respectively, which can be easily distinguished from the three strong bands of maghemite centered at 667–720 (A_{1g} modes), 500 (E_g) and 350 cm^{-1} (T_{2g}).[58–60] In addition, a second-order mode at 1421 cm^{-1} for the case of maghemite is identified.[61] The Raman spectrum of the MNP sample, along with reference spectra for maghemite and magnetite, is shown in Figure 1D. The spectrum shows good agreement between the characteristic peaks of the references and the literature, confirming that the MNP sample was composed of maghemite.

Magnetization cycles at 300 K showed that MNP exhibited superparamagnetic (SPM) behavior with negligible hysteresis and coercive fields $\leq$25 Oe (2 kA m^{-1}) (see Figure 1E and S2, Supporting Information), with saturation magnetization consistent with previous studies. UV–Vis-NIR analysis in Figure 1F confirmed the characteristic absorption of iron oxides, specifically associated with maghemite-related phases.[62–64]

2.2. Functionalization and Characterization of MNPs with Doxorubicin (DOX)

In order to use the NPs as stimuli-triggered drug delivery systems, the NPs were modified with the drug DOX. For this purpose, MNPs were functionalized in two different ways, as illustrated in Figure 1G,H: 1) the first functionalization was based on electrostatic interactions (MNP ± DOX/MNP+-DOX) and 2) second involved a disulfide bond (MNP-SS-DOX). For both functionalizations, a final concentration of 100 μM DOX was added to the NPs

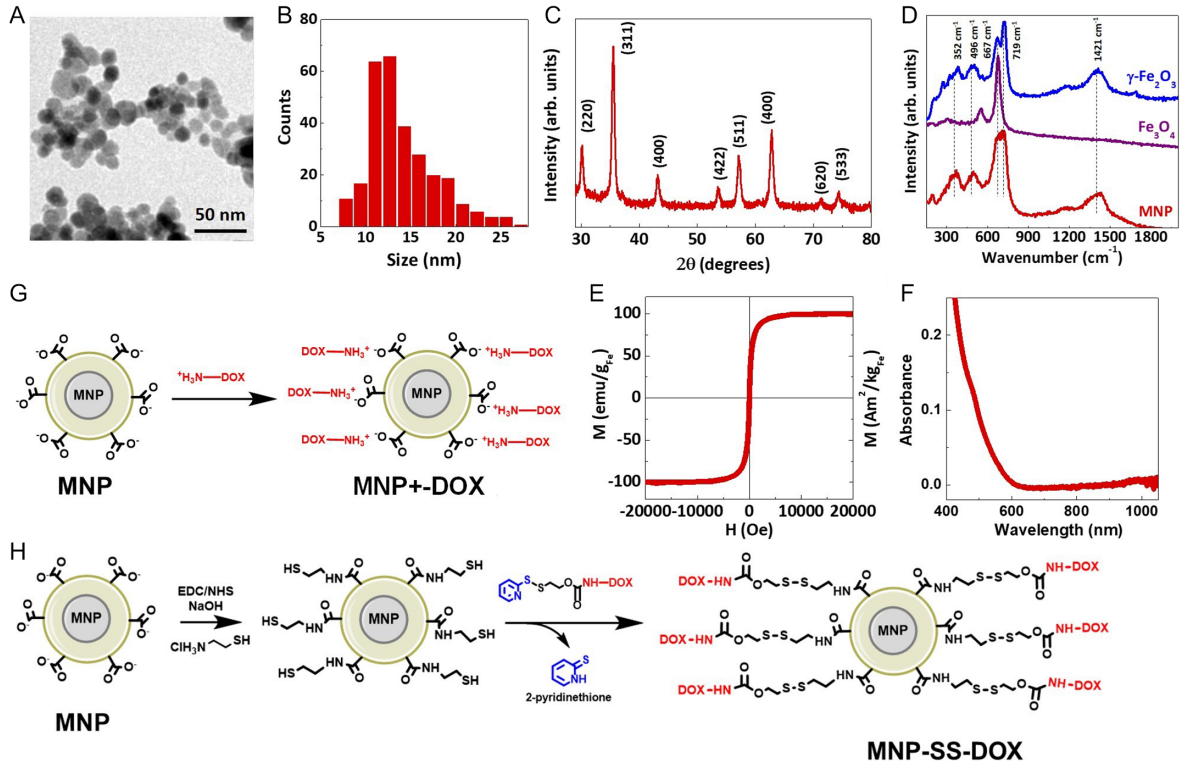

Figure 1. A) Transmission electron microscopy (TEM) image (scale bar: 50 nm) and B) size distribution of MNP sample. C) XRD of MNP sample with the corresponding diffraction maxima of a magnetic spinel structure. D) Raman spectra of the maghemite (blue) and magnetite (purple) references and the MNP sample (red). E) Field-dependent magnetization curves (M–H) of MNP at 300 K (emu $g_{Fe}^{-1} = Am^2\,kg_{Fe}^{-1}$, 1 Oe = $1000/4\pi$ A m^{-1}). F) UV–Vis-NIR spectrum of MNPs in water. General scheme of functionalization of MNPs with DOX via electrostatic interactions G) and disulfide bonds H).

(2 $mg_{Fe}\,mL^{-1}$), obtaining a binding yield of 97.7 ± 0.6% for MNP ± DOX and 75 ± 3% for MNP-SS-DOX.

DOX binding to the NPs was verified using UV–Vis-NIR spectroscopy (**Figure 2**A). While the DOX absorption band at 475–495 nm was masked by NP absorption,[65–67] subtracting the NP background revealed a DOX peak around 400 nm, consistent with prior studies on DOX-loaded IONPs.[66–69] The conjugation of DOX into the surface of MNP nanoparticles was also demonstrated by Raman spectroscopy (Figure 2B). Hence, the Raman spectra of MNP, previously identified as maghemite, were compared with those of MNP-SS-DOX and MNP ± DOX. All the peaks from MNP were observed in the functionalized samples, confirming that the structure and composition of the NPs remain stable after conjugation.

The main peaks found in pure and free DOX vary slightly in position between different studies, but mainly, there are: 1) a series of peaks at 1406, 1445 and 1575 cm^{-1} related to the skeletal ring vibrations of DOX, 2) some specific bands between 1200 and 1300 cm^{-1} attributed to bending motions of CO, COH and CH, respectively, 3) the peaks at 868 and 807 cm^{-1} are due to N—H wag, and 4) finally, the bands appearing at 440 and 465 cm^{-1} are assigned to CCO and CO deformations.[70–72] Most DOX peaks overlapped with maghemite bands, particularly at 440–465 and 1400–1450 cm^{-1}. Peaks around 1200–1300 cm^{-1} were reduced due to DOX binding and masked by MNP signals. DOX loading was confirmed by a minor peak at 876 cm^{-1}, and a clear peak at 1570 cm^{-1}, indicating successful functionalization.[73]

MNPs have a core size of 14 nm and a hydrodynamic diameter (D_h) of 112.3 nm (see Figure 2C and **Table 1**). DOX binding via a disulfide bond increased D_h to 124 nm, while electrostatic DOX binding reduced the D_h to 103.7 nm due to hydration changes. MNPs had a ζ-potential of −38 mV due to the presence of carboxyl groups on the DMSA coating,[74] ensuring stability in aqueous solutions. DOX loading increased the ζ-potential to −33 mV (MNP ± DOX) and −31 mV (MNP-SS-DOX), as in many previous works,[75–77] assuring good colloidal stability.

The saturation magnetization values of all samples were similar and consistent with previous publications,[78–80] with a slight increase observed for the functionalized MNP[81] as depicted in Figure 2D. The samples exhibit low coercivity (H_C) values (see Figure S2, Supporting Information). Magnetic measurements were not corrected. The remanent field of the superconducting magnet (≈25 Oe) falls within the range of the samples' very low or negligible coercivity, which is consistent with their SPM nature. The Zero-Field Cooling/Field Cooling (ZFC/FC) magnetic thermal curves show that the MNP curve differed slightly from the MNP-SS-DOX and MNP ± DOX curves, which were quite similar. All samples displayed a broad maximum peak, indicating a moderately broad size distribution and some degree of interparticle coupling.[82,83] The blocking temperature (T_B), represented by the maximum of the ZFC curve, was 324 K for MNP and shifted to 349 and 356 K for MNP-SS-DOX and MNP ± DOX, respectively. This increase in T_B following NP functionalization has been observed in other studies.[84] Consequently, although there were

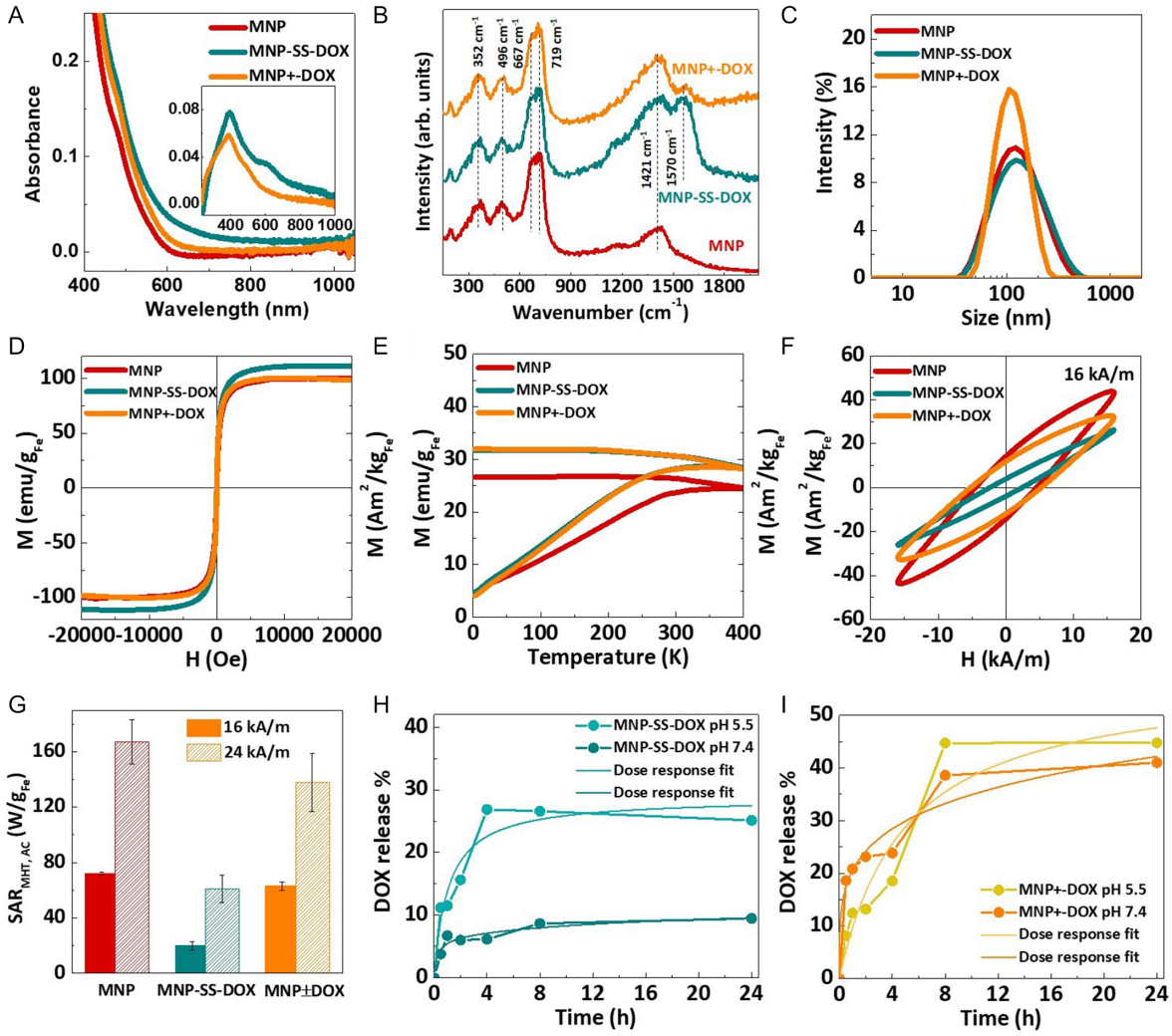

Figure 2. A) UV–Vis-NIR spectra of MNP and DOX-loaded MNP. Inset: spectra of MNP-SS-DOX and MNP ± DOX after subtracting the value of MNP at 235 nm, before the disulfide bond jump. B) Raman spectra of MNP and DOX-loaded MNP, with the main peaks highlighted. C) Hydrodynamic diameter (from DLS measurements) and D) field-dependent magnetization curves (M–H) of MNP and DOX-loaded MNP at 300 K. E) ZFC and FC curves measured under an applied magnetic field of 100 Oe. F) AC magnetization cycles at 16 kA m^{-1}, and G) magnetic $SAR_{MHT,AC}$ values of MNP and DOX-loaded MNP at two field intensities (16 kA m^{-1} solid color, 24 kA m^{-1} patterned color). The AC magnetization frequency is 100 kHz. The values represent the mean ± standard deviation from three independent measurements ($n = 3$). DOX release profiles from H) MNP-SS-DOX NPs and I) MNP ± DOX at pH 7.4 and pH 5.5, respectively.

Table 1. Summary table showing the hydrodynamic diameter, ζ-potential values, SAR values of MNP and DOX-loaded MNP under MHT and PTT in solution.

Sample	Hydrodynamic size D_h [nm]	ζ-potential [mV]	$SAR_{MHT,\ AC}$ [W g_{Fe}^{-1}]	SAR_{MHT} [W g_{Fe}^{-1}]	SAR_{PTT} [W g_{Fe}^{-1}]	$SAR_{MHT+PTT}$ [W g_{Fe}^{-1}]
MNP	112.3 ± 0.6	−38 ± 2	72 ± 1	50.6 ± 0.2	166 ± 4	239 ± 6
MNP-SS-DOX	124 ± 3	−31 ± 1	20 ± 3	38 ± 5	182 ± 7	245 ± 2
MNP+-DOX	103.7 ± 0.4	−33 ± 2	63 ± 3	43 ± 5	178 ± 7	226 ± 6

minor changes in the magnetic properties, with a slight increase in H_C and T_B, in general the magnetic properties are largely maintained after doxorubicin loading.

AC magnetometry measurements were conducted under an AMF at 100 kHz and 16 or 24 kA m^{-1}, with magnetization values normalized to the iron mass. High-frequency AMF application resulted in magnetic losses, visible as an opening of the hysteresis loop.[85,86] The AC magnetization cycles for samples at 16 and 24 kA m^{-1} are shown in Figure 2F and S3, Supporting Information, respectively. MNP and MNP ± DOX exhibited

similar AC magnetic hysteresis cycles in shape and area, while MNP-SS-DOX had a narrower cycle and smaller AC magnetic hysteresis area. This decrease in the area likely resulted from the disulfide bond inhibiting the Brownian relaxation mechanism,[87,88] a change previously noted with functionalized nanoparticles.[88,89] The obtained magnetic $SAR_{MHT,\ AC}$ varied with area at a constant field frequency of 100 kHz. MNP-SS-DOX had a lower $SAR_{MHT,\ AC}$ than bare MNP, showing a 72% reduction at 16 kA m^{-1} and 63% at 24 kA m^{-1}, while MNP ± DOX exhibited only a 12.5% reduction at 16 kA m^{-1} and 17% at 24 kA m^{-1} (see Figure 2G and Table S1, Supporting Information). DOX loading decreased heating capability more significantly with disulfide bonding, making MNP ± DOX the most effective chemo-magnetothermal agent at this point.

2.3. Macroscopic Hyperthermal Effects and DOX Release in Magneto-Photothermia Using DOX-Loaded MNPs with Calorimetric SAR Calculations in Solution

MNP and DOX-loaded MNP samples were investigated as thermal agents for MHT (AMF, 103 kHz and 20 mT), photothermia (808 nm, 0.15 W, 0.23 W cm^{-2}) and magneto-photothermia (combination of both conditions). The temperatures reached were recorded with an IR thermal camera. The temperature increase at 4 mg_{Fe} mL^{-1}, starting from room temperature, was 8–9 °C during MHT, 10–11 °C during PTT, and 18–19 °C with the combination treatment (**Figure 3**A) for MNP and DOX-loaded MNP samples. These results correspond to SAR values of 40–50 W g_{Fe}^{-1} for MHT, 170–180 W g_{Fe}^{-1} for PTT, and 225–245 W g_{Fe}^{-1} for the combination treatment across all samples (see Figure 3B and Table 1).

Same treatments were performed on the DOX-loaded MNP samples to compare with the DOX released with time. In this case, the experiments were performed at 2 mg_{Fe} mL^{-1}. Due to the significant difference in DOX release at pH 5.5 and 7.4 for MNP-SS-DOX (Figure 2H), heat-triggered release was tested at both pHs. For MNP ± DOX, with similar release as shown in Figure 2I, the study was done only at pH 7.4, limited to 30 min.

DOX release from MNP-SS-DOX was higher at pH 5.5 than at neutral pH for all treatments (15% lower at pH 7.4, Table S2, Supporting Information, and Figure 3C). Therefore, the drug release triggered by local hyperthermia treatments would be greater in cancer cells than in healthy cells, since cancer cells and tumor environments are associated with an acidic pH. At acidic pH, 59, 70% and 67% of the DOX was released for PTT, MHT, and MHT + PTT, respectively, compared to 37, 31% and 48% under physiological conditions.

DOX released by MNP ± DOX at neutral pH was 40% during PTT, 48% with MHT, and 56% in the combined application of both stimuli, being lower than those presented by MNP-SS-DOX under acidic conditions. However, MNP ± DOX exhibited larger release, with the combined application releasing 55 µM DOX (Table S2, Supporting Information), due to better DOX loading in the MNP ± DOX sample (97.7%) compared to MNP-SS-DOX (75%). Thus, although MNP ± DOX released more DOX in terms of concentration, the percentage was lower.

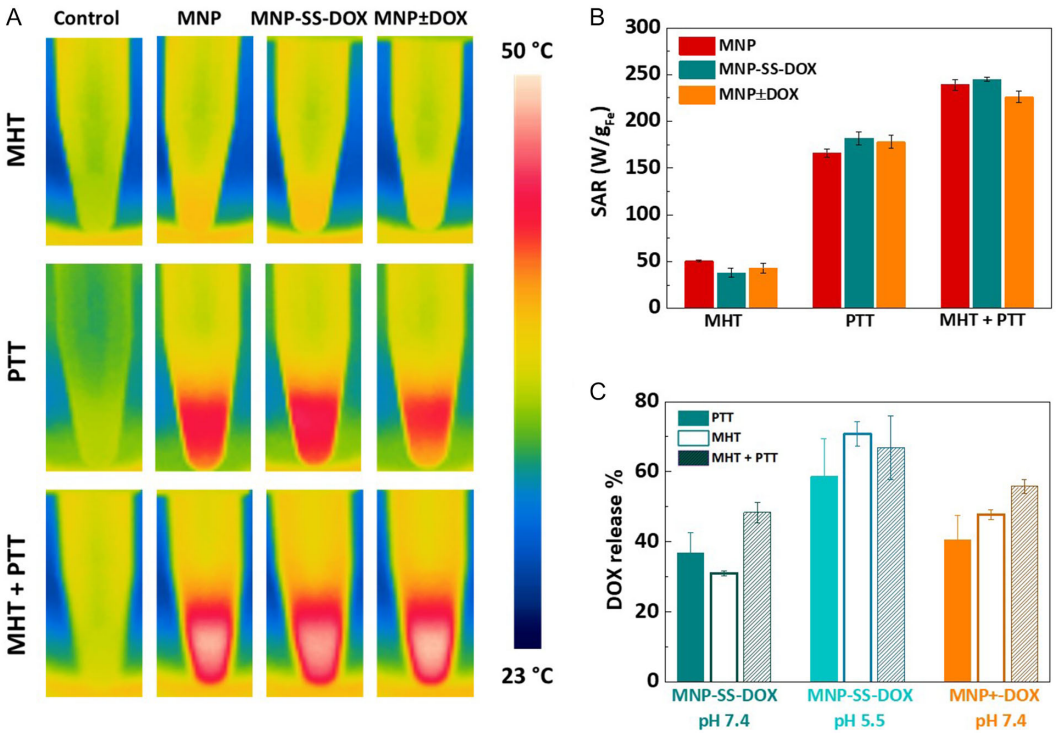

Figure 3. A) Thermal infrared images of the MNP and functionalized samples under PTT, MHT and combined application taken at the end of each protocol till steady state. B) SAR values under PTT, MHT and combined protocol. C) Percentage of DOX released upon PTT, MHT and combined application for the MNP ± DOX and MNP-SS-DOX samples at neutral and acidic pH. Bars are presented as the mean ± standard error propagation ($n = 3$).

In general, thermal treatment significantly enhanced DOX release in all cases at short times compared to passive release after 24 h. Similar increases in drug release have been reported in previous studies.[90–92] This study further confirms that the disulfide bond is thermolabile,[93] enabling efficient heat-triggered DOX release. Notably, although MHT consistently resulted in the smallest heating capability, it elicited greater drug release than PTT in both MNP-SS-DOX at pH 5.5 and MNP ± DOX at pH 7.4. This suggests that drug release may not depend exclusively on heat or pH conditions but could also involve additional underlying mechanisms.

2.4. DOX-Loaded MNP as Efficient Agents for Magneto-Photothermal-Triggered Intracellular Drug Delivery

To initiate the *in vitro* studies, the cytotoxicity of NPs was assessed in MCF-7 cells (breast cancer cells). Cells were incubated with MNPs and DOX-MNPs (0.1 $mg_{Fe}\,mL^{-1}$) for 24 h, and cell viability was measured using the Alamar Blue assay (**Figure 4**A). The results showed high biocompatibility of DMSA-coated MNPs, consistent with previous studies. Both MNP ± DOX and MNP-SS-DOX exhibited negligible toxicity, maintaining viability near 98%, while free DOX (5 µM) reduced viability by 44%. Under acidic conditions typical of the lysosomal environment, MNP ± DOX released 45% of its DOX payload, and MNP-SS-DOX released 26%, both showing lower DOX release than the free drug, which correlated with higher cell viability. These findings indicate that MNPs serve as biocompatible nanocarriers that reduce DOX cytotoxicity through controlled release.

The antiproliferative effects of free DOX on MCF-7 cells were further evaluated across a concentration range of 0–100 µM, over 24, 48 and 72 h (Figure S4, Supporting Information). A substantial decrease in cell viability was observed at high concentrations, although cell death occurs at all concentrations except for 0.5 µM. Complete eradication occurred at 50 µM after 48 h and at 20 µM after 72 h, with no activity observed above 100 µM at 24 h. The IC_{50} was 5–6 µM at 24 h and less than 1 µM at 48 and 72 h, consistent with previous studies.[94–98]

Quantitative particle uptake was assessed by measuring iron content using inductively coupled plasma optical emission spectrometry (ICP-OES) at different concentrations. As shown in

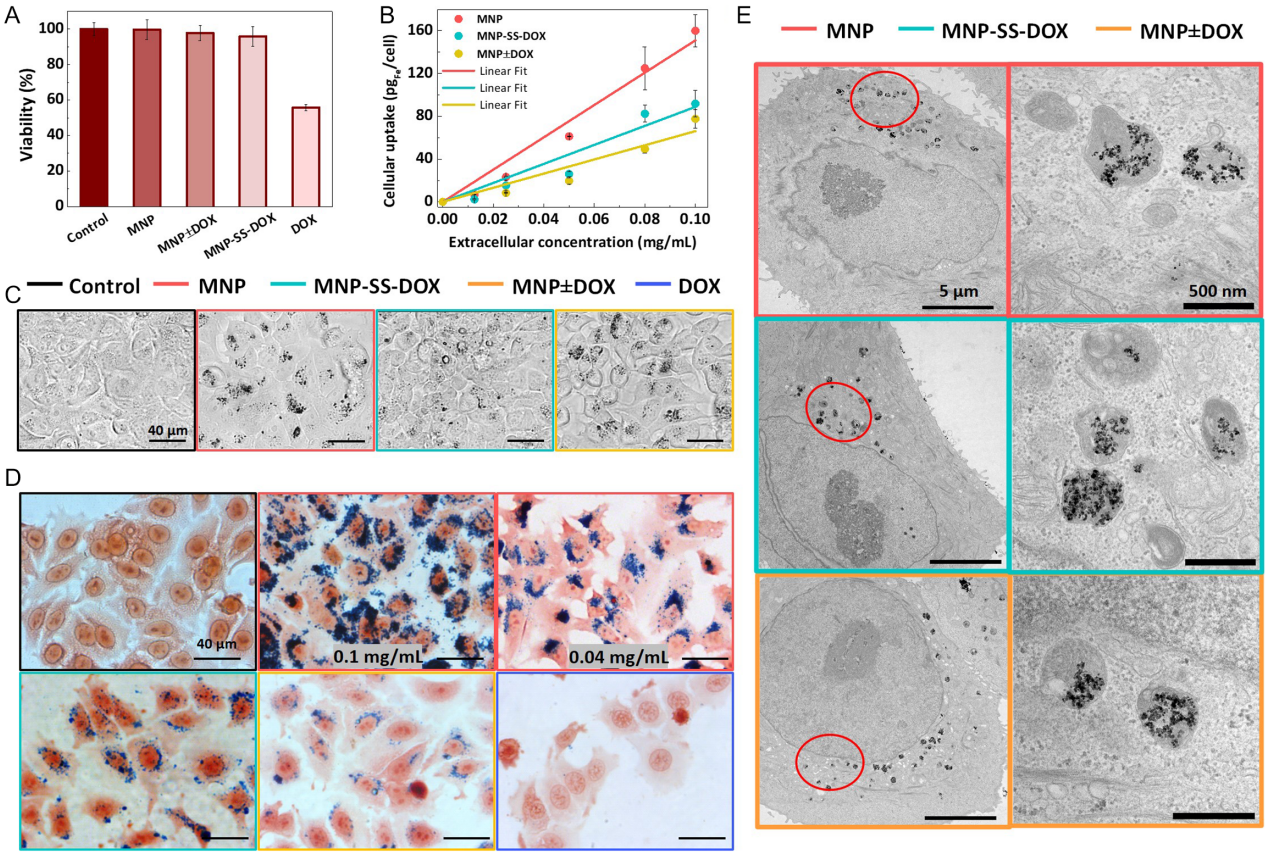

Figure 4. A) Biocompatibility study and B) cellular uptake in MCF-7 cells of MNP and DOX-loaded MNPs after 24 h of incubation (0.1 $mg_{Fe}\,mL^{-1}$) and free DOX at 5 µM. The values represent the mean ± standard deviation from three independent measurements ($n = 3$). C) MCF-7 cells visualized by bright-field microscopy. Black dots correspond to aggregates of NPs. Cells were incubated with 0.04 $mg_{Fe}\,mL^{-1}$ of MNP and 0.08 $mg_{Fe}\,mL^{-1}$ of DOX-loaded MNP for 24 h. The scale bar represents 40 µm. D) Cells were stained with Prussian Blue and Neutral Red dye for visualization by bright-field microscopy. Cells were incubated with 5 µM of DOX, 0.1 $mg_{Fe}\,mL^{-1}$ of DOX-loaded MNP, and 0.04 $mg_{Fe}\,mL^{-1}$ of MNP. The scale bar represents 40 µm. E) TEM images of MCF-7 cells incubated with 0.04 $mg_{Fe}\,mL^{-1}$ of MNP and 0.08 $mg_{Fe}\,mL^{-1}$ of DOX-loaded MNPs (scale bars = 5 µm (left) and 500 nm (right)).

Figure 4B, cellular uptake was highest for MNPs without the drug, followed by MNP-SS-DOX and MNP ± DOX. MNP-SS-DOX had a lower negative charge, which could aid internalization, but its larger size might hinder uptake. Consequently, the drug-loading process affected internalization without showing any trend related to size or charge, though uptake remained dose-dependent, as reported in the literature.[99,100]

MNP incorporation into MCF-7 cells was monitored using optical microscopy (Figure 4C). Bright-field microscopy revealed MNPs as black cytoplasmic spots outside the nucleus. Prussian Blue staining identified NPs as blue precipitates in the perinuclear zone, while Neutral Red staining indicated normal cell morphology without blue granules in the nucleus, as depicted in Figure 4D. At a concentration of 0.1 $mg_{Fe}\,mL^{-1}$ MNPs exhibited higher cellular uptake than MNP-SS-DOX and MNP ± DOX, corroborating the ICP-OES results. At 0.04 $mg_{Fe}\,mL^{-1}$, iron levels matched those of DOX-loaded MNPs (Figure S5 and Table S3, Supporting Information). Treatment with free DOX increased cell death, as evidenced by larger attached cells with nuclear alterations, including dispersed chromatin and absent nucleoli, likely due to DOX-induced cell cycle arrest.[101,102] Transmission electron microscopy (TEM) images (Figure 4E) revealed clustered NPs within endosomal compartments and indicated similar NP concentrations across samples.[99,103]

For experiments comparing MNPs with DOX-loaded MNPs, 0.04 $mg_{Fe}\,mL^{-1}$ was used for MNP and 0.08 $mg_{Fe}\,mL^{-1}$ for the nanocarriers. MNP-SS-DOX and MNP ± DOX showed similar internalization, with 0.08 $mg_{Fe}\,mL^{-1}$ corresponding to 0.04 $mg_{Fe}\,mL^{-1}$ of MNP, based on the linear fits in Figure S5, Supporting Information.

2.5. Compositional Stability and Structural Characterization of MNPs in Solution and in Tumor Cells

An advanced characterization of the structural details of the NPs, both in solution and after internalization in cells, was performed using X-ray absorption spectroscopy (XAS) at the Fe K-edge (7112 eV). This is an excellent tool due to its element selectivity, discriminating between magnetite and maghemite, and its sensitivity to high dilutions as can occur in cells.[104–106] The Fe K-edge XAS spectra were measured at the BM23 beamline of the European Synchrotron Radiation Facility (ESRF Grenoble, France).

The XAS spectra can be divided into two distinct regions: the X-ray absorption near edge structure (XANES), which spans ≈100 eV beyond the absorption edge and is highlighted in light blue in Figure S7, Supporting Information, and the extended X-ray absorption fine structure (EXAFS), depicted in green. **Figure 5**A presents the Fe K-edge XANES spectra of MNP samples in solution and cells, compared with Fe_3O_4 and γ-Fe_2O_3 references. While both phases share an inverse spinel structure, γ-Fe_2O_3 differs due to cation vacancies at octahedral sites. XANES identifies these phases by probing the Fe oxidation states: +3 for maghemite and a mix of +2/+3 for magnetite, shifting the Fe^{3+} absorption edge to higher energies.[106,107] All NPs were primarily maghemite in both solution and cell samples, confirming Raman results.

To quantitatively study the coordination number, interatomic distance and structural disorder the EXAFS region was analyzed. The first three shells corresponding to Fe—O, Fe_O—Fe_O bonds (in octahedral positions) and Fe_T-$Fe_{T,O}$ (in octahedral O and tetrahedral T positions) were analyzed (**Table 2**). As shown in Figure 5B,

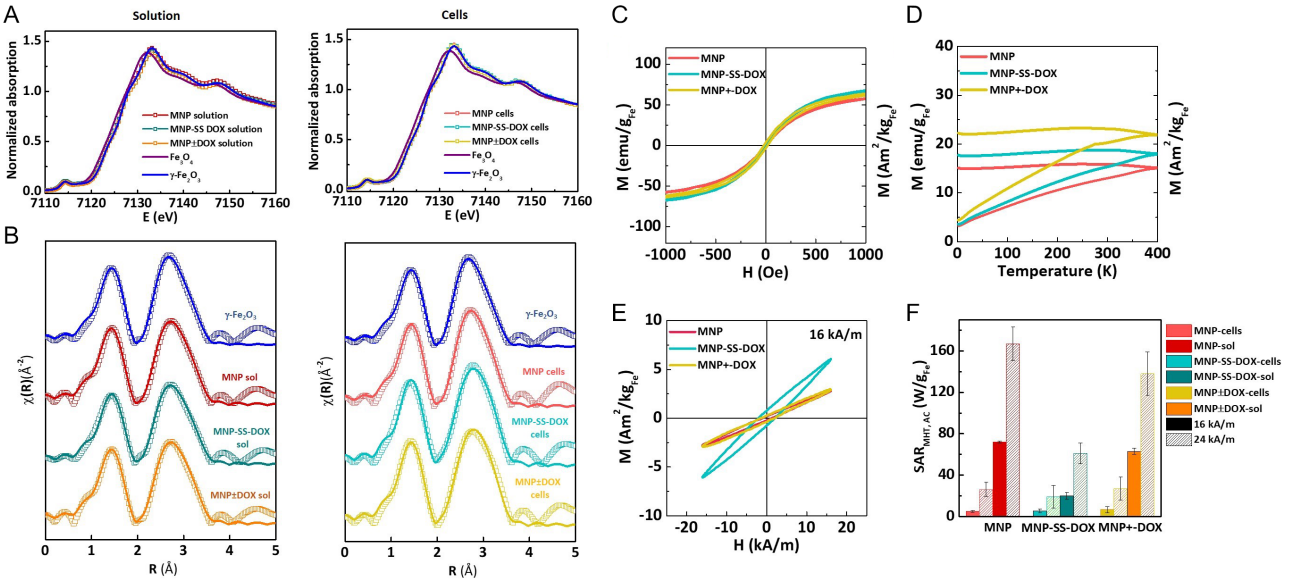

Figure 5. A) XANES spectra at the Fe K-edge (7112 eV) of the MNP samples in solution and cells, along with magnetite (Fe_3O_4) and maghemite (γ-Fe_2O_3) references. B) R-space of the EXAFS spectra after Fourier transform (FT) with k^2-weighting for the γ-Fe_2O_3 reference and MNP samples in both solution and cells. C) Magnetization curves at 300 K and D) ZFC/FC curves measured under an applied magnetic field of 100 Oe of MNP and DOX-loaded MNP in cells. E) AC magnetization cycles at 16 kA m^{-1} and 100 kHz of MNP and DOX-loaded MNP in cells. F) Graphical representation of the magnetic $SAR_{MHT,\,AC}$ values of the samples in both solution and internalized in cells. The values represent the mean ± standard deviation from three independent measurements ($n = 3$).

Table 2. Tables collecting the coordination number (N), interatomic distance (R) and Debye–Waller factor (σ^2) of the first three shells, corresponding to the Fe—O, Fe_O—Fe_O and Fe_T—$Fe_{T,O}$ bonds.

1st shell Fe_O-Fe_O	N		R [Å]		σ^2 [Å^2]	
Sample	Solution	Cells	Solution	Cells	Solution	Cells
γ-Fe_2O_3	5.25 ± 0.03		1.96 ± 3 E−3		0.012 ± 5 E−4	
MNP	5.05 ± 0.03	5.42 ± 0.02	1.95 ± 3 E−3	1.96 ± 3 E−3	0.011 ± 4 E−4	0.011 ± 4 E−4
MNP-SS-DOX	4.38 ± 0.03	5.63 ± 0.06	1.96 ± 4 E−3	1.96 ± 4 E−3	0.011 ± 5 E−4	0.011 ± 9 E−4
MNP ± DOX	5.08 ± 0.03	5.60 ± 0.03	1.96 ± 2 E−3	1.96 ± 3 E−3	0.012 ± 5 E−4	0.011 ± 5 E−4
2nd shell Fe_O-Fe_O	N		R [Å]		σ^2 [Å^2]	
Sample	Solution	Cells	Solution	Cells	Solution	Cells
γ-Fe_2O_3	3.75 ± 0.04		3.00 ± 3 E−3		0.013 ± 4 E−4	
MNP	3.42 ± 0.04	4.10 ± 0.04	3.00 ± 4 E−3	3.01 ± 3 E−3	0.013 ± 4 E−4	0.014 ± 4 E−4
MNP-SS-DOX	3.38 ± 0.03	4.64 ± 0.06	3.01 ± 4 E−3	3.01 ± 5 E−3	0.013 ± 5 E−4	0.016 ± 1 E−3
MNP ± DOX	3.61 ± 0.03	4.31 ± 0.03	3.00 ± 2 E−3	3.01 ± 5 E−3	0.014 ± 5 E−4	0.015 ± 5 E−4
3rd shell Fe_T-$Fe_{T,O}$	N		R [Å]		σ^2 [Å^2]	
Sample	Solution	Cells	Solution	Cells	Solution	Cells
γ-Fe_2O_3	8.25 ± 0.05		3.46 ± 3 E−3		0.012 ± 5 E−4	
MNP	8.16 ± 0.04	10.08 ± 0.04	3.46 ± 4 E−3	3.47 ± 3 E−3	0.012 ± 4 E−4	0.012 ± 4 E−4
MNP-SS-DOX	7.39 ± 0.04	11.9 ± 0.1	3.47 ± 4 E−3	3.48 ± 5 E−3	0.011 ± 5 E−4	0.012 ± 7 E−4
MNP ± DOX	7.91 ± 0.04	11.80 ± 0.05	3.47 ± 3 E−3	3.47 ± 3 E−3	0.012 ± 4 E−4	0.012 ± 4 E−4

the coordination number decreased in the solution samples compared to the reference, due to missing neighbors at the surface of the NPs and maybe to self-absorption phenomena.[106,108] However, the coordination number in the cells samples was a bit higher than the coordination number of the γ-Fe_2O_3 reference in all cases, likely due to the aggregation that the NPs undergo due to endosomal confinement once they were internalized in the cells. This increase was even higher in the case of MNP-SS-DOX. The Fe—O and Fe—Fe bond lengths from the Fourier transform of the EXAFS spectra agreed with the theoretical values (1.96, 3.00 and 3.46 Å) and the literature values.[109,110]

The Debye–Waller (DW, σ^2) factor, which reflects the structural disorder, was consistent with the reference values, with slight variations in the first shell. Moreover, the DW factor remains constant after cellular uptake of the NPs, except for the second shell where a slight increase was observed. In summary, EXAFS analysis showed consistent bond distances and structural disorder, with minor changes in coordination number, suggesting that maghemite NPs remain stable after functionalization and tumor cell uptake.

The magnetic properties of the NPs inside cells have been analyzed (Figure 5C,D). The magnetic hysteresis curves at 300 K for internalized NPs closely resembled those in solution but showed an ≈20% reduction in magnetization saturation. This decrease is likely due to NP aggregation within cellular compartments, where dipolar interactions between closely packed NPs can lead to spin disorder and partial magnetic frustration, reducing the alignment efficiency of magnetic moments under an external field.[18,87,111,112] While coercivity values remained low, ZFC/FC measurements in cells displayed flattened curves with a broad maximum around 300–400 K, indicating a higher T_B after endosomal internalization. Overall, despite a slight reduction in signal, the magnetic properties were largely preserved inside cells.[112]

The magnetic heating capability of NPs in cells was assessed via magnetic $SAR_{MHT,\ AC}$ at same conditions as those in solution (Figure 5E,F). Figure 5E shows the AC curves for MNP and DOX-loaded MNPs in cells, which exhibited significant changes in sigmoidal shape and specific magnetization compared to water dispersion (Figure 2F). For instance, at 16 kA m^{-1}, MNPs in cells had 15 times lower magnetization than in solution. MNP-SS-DOX retained a cyclic shape similar to that in solution but exhibited reduced magnetization in cells. This sample also showed partially suppressed Brownian relaxation even in solution due to sulfide bonding functionalization. This functionalization may also prevent NP aggregation through steric hindrance, possibly explaining why MNP ± DOX had higher magnetization than MNP.

At 16 and 24 kA m^{-1}, MNP-SS-DOX largely retained its cycle shape, while MNP and MNP ± DOX showed reduced coercivity, remanence, and magnetic $SAR_{MHT,\ AC}$ values. Internalization caused significant magnetic $SAR_{MHT,\ AC}$ drops (see Figure 5F, S7 and Table S3, Supporting Information): 93% and 84% at 16 and 24 kA m^{-1} for MNP, 90% and 80% for MNP ± DOX, and smaller reductions of 73% and 67% for MNP-SS-DOX, likely due to functionalization limiting Brownian rotation and aggregation. All NPs experienced reduced magnetic losses, attributed to clustering-induced dipolar interactions and increased media viscosity of the surrounding medium.[16,80,111,113,114] The results suggest inhibited Brownian rotation and possible Néel relaxation effects, as seen in decreased magnetization in SQUID measurements. It can be concluded that NPs undergo a large reduction in

magnetic heat release upon internalization. Consequently, all NPs displayed similarly low SAR values, ranging from 5 to 7 W g_{Fe}^{-1}.

2.6. Trimodal Chemo-Magneto-Photothermal Treatment Mediated by DOX-Loaded MNPs

Achieving therapeutic temperatures uniformly throughout the tumor region remains a challenge, and hyperthermia alone rarely achieves complete tumor shrinkage. Similarly, chemotherapy often lacks localized action and may lead to treatment resistance. Combining thermal treatments with chemotherapy addresses these limitations, enhancing tumor cell eradication. In this study, the combination of thermal treatments with local chemotherapy was examined, both individually and as part of a trimodal treatment approach (MHT + DOX, PTT + DOX, and MHT + PTT + DOX). For this, cells were incubated with NPs for 24 h, harvested, and reseeded after treatment (refer to the Experimental Section, Section 5). Incubation concentrations were adjusted to ensure equivalent final iron content per cell: 0.04 $mg_{Fe}\,mL^{-1}$ for MNPs and 0.08 $mg_{Fe}\,mL^{-1}$ for DOX-loaded MNPs. Final temperature increases during treatments were obtained. Notable differences were observed between treatments, with minimal variation among samples. Control cells showed slight temperature rises during MHT, consistently lower than those observed in treated samples. Both DOX-loaded MNPs and MNPs generated heat under external stimuli. Temperature increases (ΔT °C) during MHT were generally below 3 °C, while PTT resulted in increments around 4 °C as shown in **Figure 6**A. Dual treatments caused temperature rises of ≈8–9 °C across all samples from 37 °C.

MNP-cells exposed to MHT showed significant reductions in viability, with 86% viability at 24 h for MNPs and a larger reduction (61%) after 48 h, as shown in Figure 6B. At 72 h, viability increased to 84%, suggesting the need for reapplying MHT before this time. Functionalized samples showed greater reductions, with viability dropping to 70% at 24 h and further to 63% at 72 h, as DOX inhibited the initial proliferation observed with MNPs alone.

DOX-loaded MNPs released 1.2 μM of DOX under MHT and acidic conditions, showing synergistic effects with MHT at 24 h (drug combination index, DCI = 0.97–0.98) but antagonistic effects after 48 and 72 h, likely due to MNP-induced proliferation. Combined treatments showed higher viability than literature values,[115,116] attributed to milder clinical conditions. For example, higher viability reductions in prior studies required multiple cycles of MHT or higher AMF parameters. Our system achieved similar proportional decreases but under safer conditions, demonstrating high biocompatibility.

PTT with MNPs reduced viability to 78% at 48 h, followed by recovery to 100% at 72 h, suggesting the need for reirradiation after 48 h. DOX-loaded NPs reduced viability by ≈50% at 48 and 72 h with MNP-SS-DOX showing slightly better results at early time points (see Figure 6C).

The literature typically employs more aggressive PTT irradiation conditions, which, although reducing tumor cell viability to a greater extent, may not be suitable for clinical practice. One study shows that when cells were incubated with 0.15 $mg_{Fe}\,mL^{-1}$ DOX-NPs and irradiated at 0.8 W cm^{-2}, viability dropped to 40% at 48 h. However, higher powers of 1.1 and 1.3 W reduced viability to below 10%.[91] In contrast, our results showed a maximum reduction of 51% at 48 h with much lower laser power (0.15 W, 0.23 W cm^{-2}), demonstrating similar efficacy. Other studies report up to 80% viability reduction with PTT and DOX, but using higher powers of 1–2 W cm^{-2}.[93,117] Additionally, while some PTT-triggered drug delivery systems reduce viability,[91] others, like ours, offer excellent biocompatibility.[117]

In the trimodal treatment (Figure 6D), the control cells were minimally affected by the combined hyperthermia treatment, with viability slightly decreasing to 96% after 72 h. Viability decreased under all conditions. Combined treatment caused a more pronounced reduction in viability compared to MHT or PTT alone. Cell viability dropped 44% at 48 h but increased to 61% at 72 h, possibly due to MNP-induced proliferation.

When DOX was combined with hyperthermia mediated by MNPs, cell viability decreased by 50% within 24 h and eradicated 65–70% of cancer cells after 48 and 72 h. MNP ± DOX demonstrated slightly greater efficacy than MNP-SS-DOX, suggesting that MHT was more effective than PTT at these concentrations.

Trimodal chemo-magneto-photothermal treatment was synergistic only within the first 24 h, as indicated by DCI values of 0.58 and 0.63 for MNP-SS-DOX and MNP ± DOX, respectively, but proved more effective than free DOX at 1 μM in a single cycle. Free DOX reduced cell viability to 88%, 42%, and 34% at 24, 48, and 72 h, respectively. In contrast, trimodal treatment lowered cell viability to 50% at 24 h, further decreasing to 27%–35% at 48 h and 32%–35% at 72 h. The use of nanocarriers may then provide additional benefits, including protection of DOX, prolonged circulation time, and targeted release at the tumor site. This approach thus reduced the likelihood of drug resistance and minimized exposure of healthy tissues to the cytotoxic effects of DOX.

2.7. Mechanisms of Cell Death Induced by Trimodal Treatment

To investigate the type of cell death induced by the combined MHT + PTT treatment, flow cytometry analysis of annexin V-FITC and propidium iodide (PI) was performed (**Figure 7** and Table S5, Supporting Information). The control conditions showed 15% cell death, likely due to the staining protocol (see Figure 7A). No significant differences were observed following nanoparticle internalization or between treated and untreated cells under nonthermal conditions, confirming the safety and biocompatibility of magneto-photothermal treatment and MNP/DOX-loaded MNPs. Cells treated with free DOX or combined hyperthermia with NPs showed significant decreases in viability, particularly for DOX-loaded MNPs (Figure 7B). At 4 μM, free DOX resulted in ≈35% cell death, primarily through early apoptosis (≈16%), with necrosis or late apoptosis contributing to ≈16%. While both death pathways are common for chemotherapeutics, our results suggest apoptosis as the main mechanism. Not all NPs were internalized, so internalized DOX concentrations might be higher for free DOX than for DOX-loaded NPs.

Treated cells incubated with MNPs primarily showed necrosis or late apoptosis (≈18%), with minimal early apoptosis. Higher thermal doses typically increase necrotic cell death,[118] and the

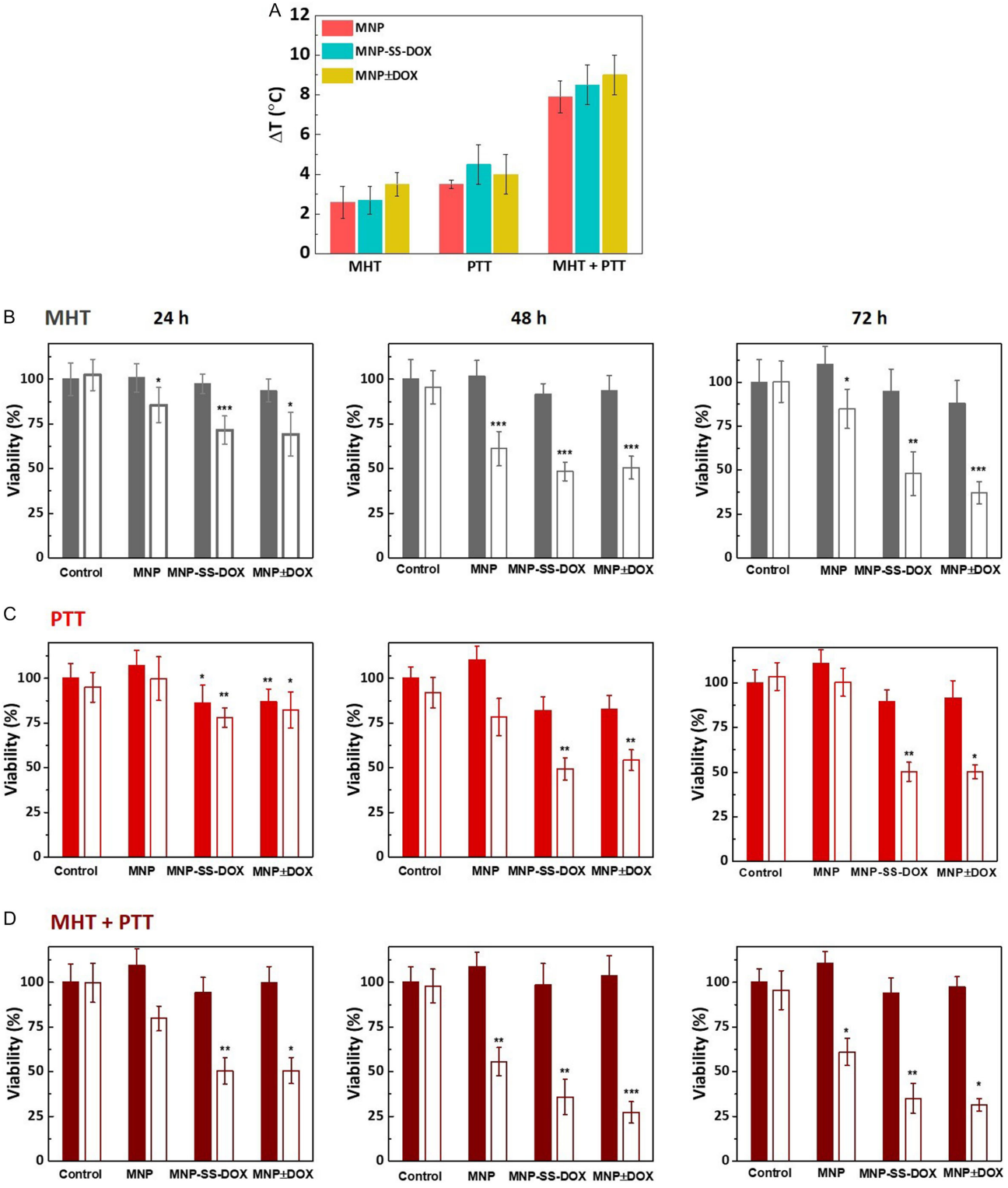

Figure 6. A) Average temperature rise measured with the IR-thermal camera during MHT, PTT, and dual treatments, respectively. Viability study after B) MHT, C) PTT and D) MHT + PTT treatments of MNP (0.04_{Fe}mg mL^{-1}) and DOX-loaded MNP (0.08 mg_{Fe} mL^{-1}) at 24, 48 and 72 h. Solid bars indicate untreated control and labeled cells, while hollow bars represent the same conditions but under thermal treatments. The data are presented as the mean ± standard deviation of three separate experiments ($n = 3$). Statistical significance was assessed using a *t*-test for each value versus its control: $*p < 0.05$, $**p < 0.01$, $***p < 0.001$.

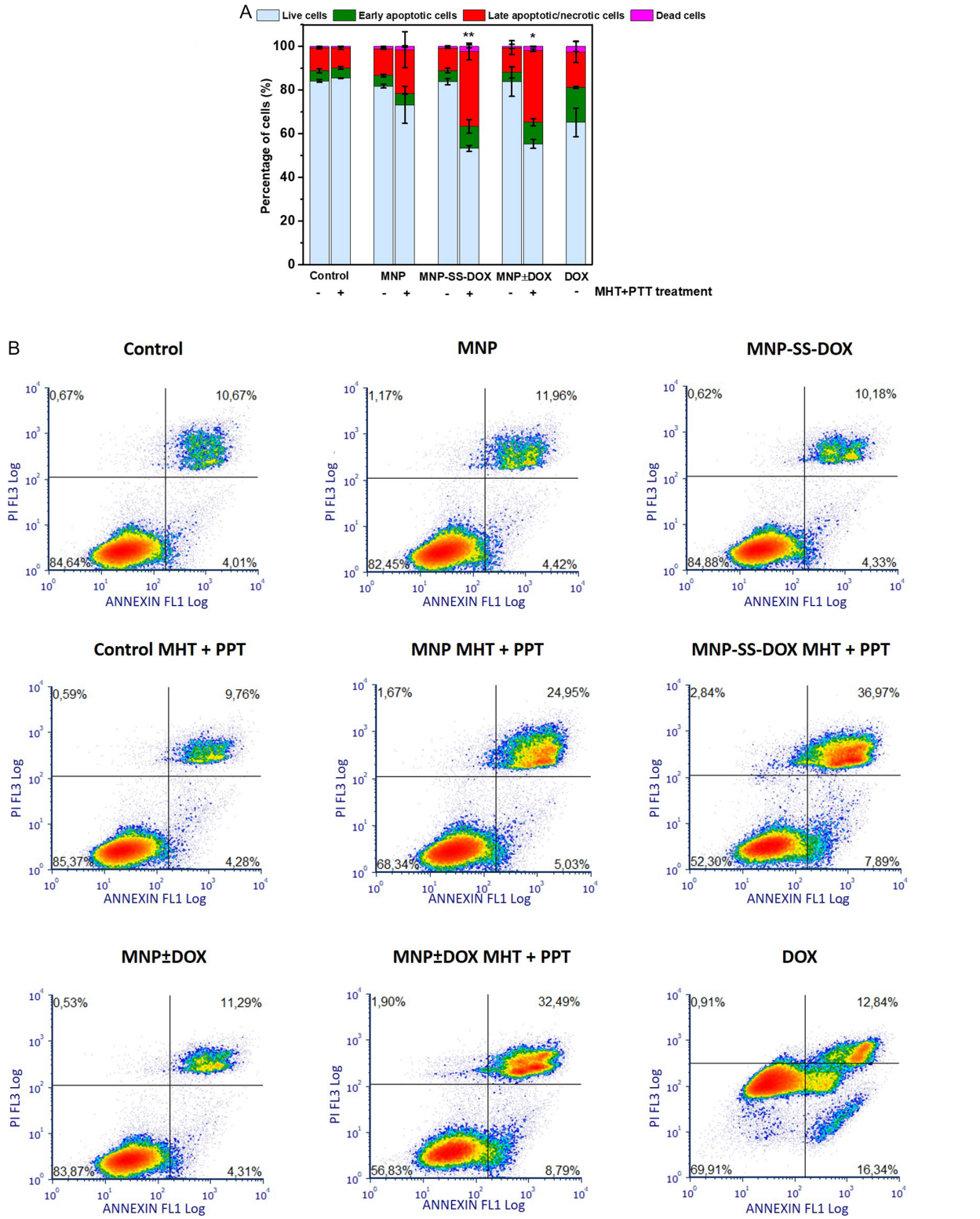

Figure 7. A) Graphical representation of the percentages of cells in each stage obtained by flow cytometry analysis of apoptosis/necrosis assay 48 h postDUAL (MHT + PTT) treatment in MCF-7 cells. A positive sign indicates the application of the MHT + PTT thermal treatment, while a negative sign represents the absence of thermal treatment. In light blue (live cells), green (early apoptotic cells), red (necrotic/late apoptotic cells) and in pink (other dead cells). The data are presented as the mean ± standard deviation of three separate experiments ($n = 3$). Statistical significance was assessed using ttest of each value versus its control. *$p < 0.05$, **$p < 0.01$, ***$p < 0.001$. B) Representative graphs from one of the flow cytometry repetitions analyzing the apoptosis/necrosis assay 48 h postDUAL treatment.

8 °C rise for MNPs likely contributed to this effect, consistent with other hyperthermia studies. When cells were treated with DOX-loaded MNPs, a higher percentage of cell death was achieved following combined thermal treatment, presenting higher cytotoxicity than MNP or DOX alone. Both MNP-SS-DOX and MNP ± DOX increased early apoptosis (10%), but most cells were in necrosis or late apoptosis (≈35%), suggesting that high temperatures drive necrosis while DOX triggers early apoptosis.

2.8. Intracellular Localization of DOX Before and after the Thermal Treatments

Cells labeled with MNPs, DOX-loaded MNPs, and control cells were stained with Hoechst for nuclear visualization (blue), mouse antiLAMP-2 followed by antimouse Alexa Fluor 647 for lysosomes (green), and the natural fluorescence of DOX for its localization (red) (**Figure 8**A). In both MNP-SS-DOX and MNP ± DOX groups, DOX predominantly localized within lysosomes, although not all lysosomes contained DOX-loaded NPs. Conversely, in treated samples, DOX was mostly dispersed throughout the cytoplasm, finally reaching the nucleus. Figure 8B further illustrates that in untreated cells, DOX remained confined to endo/lysosomal compartments and was absent from the nuclear region. Upon thermal treatment, DOX also filled the nuclear region. This redistribution is consistent with other works.[93,119,120] Furthermore, in treated samples, DOX was also detectable in the cytoplasm, confirming that thermal treatment facilitated its release from lysosomal compartments. This lysosomal escape has been reported in other studies.[82,121] Collectively, the data indicate that, following treatment, DOX was released from the NPs, escaped from intracellular compartments, and successfully reached the nucleus, where it could bind to DNA and exert its cytotoxic effects. After washing and fixation, only cells minimally exposed to thermal and chemotherapy treatments remained viable, as dead cells were removed. This is consistent with the observation that cells treated with thermal DOX-loaded MNPs were difficult to locate after the experiment.

In contrast, in the DOX control sample, the nucleus was completely invaded by DOX.[120] Furthermore, a reduction in lysosomal expansion within the cytoplasm was evident, indicating possible cytoplasmic retraction and a rounded shape, which could indicate that cells were undergoing cell death processes[122] This same trend was observed in the treated cells, however, detecting high nuclear concentrations of DOX proved more challenging, likely because these cells did not survive the treatment.

Therefore, it can be concluded that DOX initially colocalized with NPs in endo/lysosomes. Thermal treatment released DOX from NPs, enabling nuclear entry. Some DOX remained in NPs, while cells with higher levels were likely eradicated.

3. Discussion

This study underscores the potential of maghemite (γ-Fe_2O_3) nanoparticles (MNPs), synthesized via coprecipitation, as versatile and effective agents for cancer treatment. By developing and optimizing an innovative therapeutic strategy, chemo-magneto-PTT, we demonstrate their ability to achieve significant efficacy at clinically relevant low doses, paving the way for innovative and more efficient cancer therapies. These particles exhibited optimal physico-chemical properties and stability in the biological environment, making them suitable for multifunctional therapeutic applications when functionalized with DOX. Functionalization was achieved through electrostatic interactions (MNP ± DOX) or disulfide bonds (MNP-SS-DOX), resulting in high drug-loading efficiencies of 97.7% and 75%, respectively, based on previous findings on magnetic nanocarriers designed for drug delivery.[36,37]

The MHT and PTT thermal treatments generated temperature increases of up to 19 °C, with SAR values reaching 225–245 $W\,g_{Fe}^{-1}$ in combined dual mode. It is important to note that these thermal conditions were applied at safe limits: MHT was performed at 20 mT and 103 kHz, well below the clinical limits, with $H \times f = 1.6 \times 10^9\ A\,m^{-1}\,s^{-1}$,[123] and PTT was conducted at 808 nm with laser power densities of 0.23 $W\,cm^{-2}$, within safe tolerable ranges.[124] These mild thermal conditions effectively triggered pH-sensitive DOX release, particularly for MNP-SS-DOX, where release rates exceeded 70%. Enhanced release in acidic conditions highlights the potential of the system to exhibit a higher activity in tumor microenvironments. Notably, MHT promoted greater DOX release than PTT for MNP-SS-DOX, suggesting additional mechanisms might play a role.

Cellular uptake studies demonstrated efficient internalization of MNPs and DOX-loaded MNPs into MCF-7 cells, with TEM confirming their presence in endosomal compartments. Drug loading, rather than nanoparticle size or charge, was the key factor influencing internalization, which followed a dose-dependent pattern, as described in the literature.[99,100] The internalization of DOX-loaded MNPs was measured at 40–80 pg per cell, indicating a high degree of internalization.

Advanced structural analysis via XAS indicated that the structural integrity of MNPs was retained after cellular uptake, with minor aggregation-associated decreases in saturation magnetization. These results highlight the ability of functionalized nanoparticles to preserve their structural and functional properties after uptake, ensuring stable functionality without immediate degradation. Although advanced synchrotron techniques have been used to monitor MNPs within biological environments,[125–129] this analysis has never been applied to DOX-loaded MNPs.

Cytotoxicity assays revealed that MNPs mitigated the off-target effects of DOX, with MNP ± DOX and MNP-SS-DOX showing ≈98% cell viability compared to a 44% reduction for equivalent free DOX. Combined MHT and PTT treatments significantly reduced cell viability, achieving 27%–35% viability at 72 h, outperforming free DOX. The trimodal treatment, resulted synergistic in the 24 h and outperformed free DOX (1 μM), reducing viability to 50%, 27–35%, and 32–35% at 24, 48 and 72 h, compared to 88%, 42%, and 34% for free DOX. This indicates that the nanocarriers protect DOX integrity, prolong its circulation, and enable targeted release of intact, active drug in tumor sites. This strategy also mitigates drug resistance in cancer cells and minimizes DOX exposure to healthy tissue.

Flow cytometry analyzes showed that DOX-loaded MNPs induced cell death predominantly through necrosis and late apoptosis, consistent with the thermal damage and controlled drug release observed.[97,130,131] Lysosomal release of DOX was observed following thermal treatment, with DOX dispersing into the

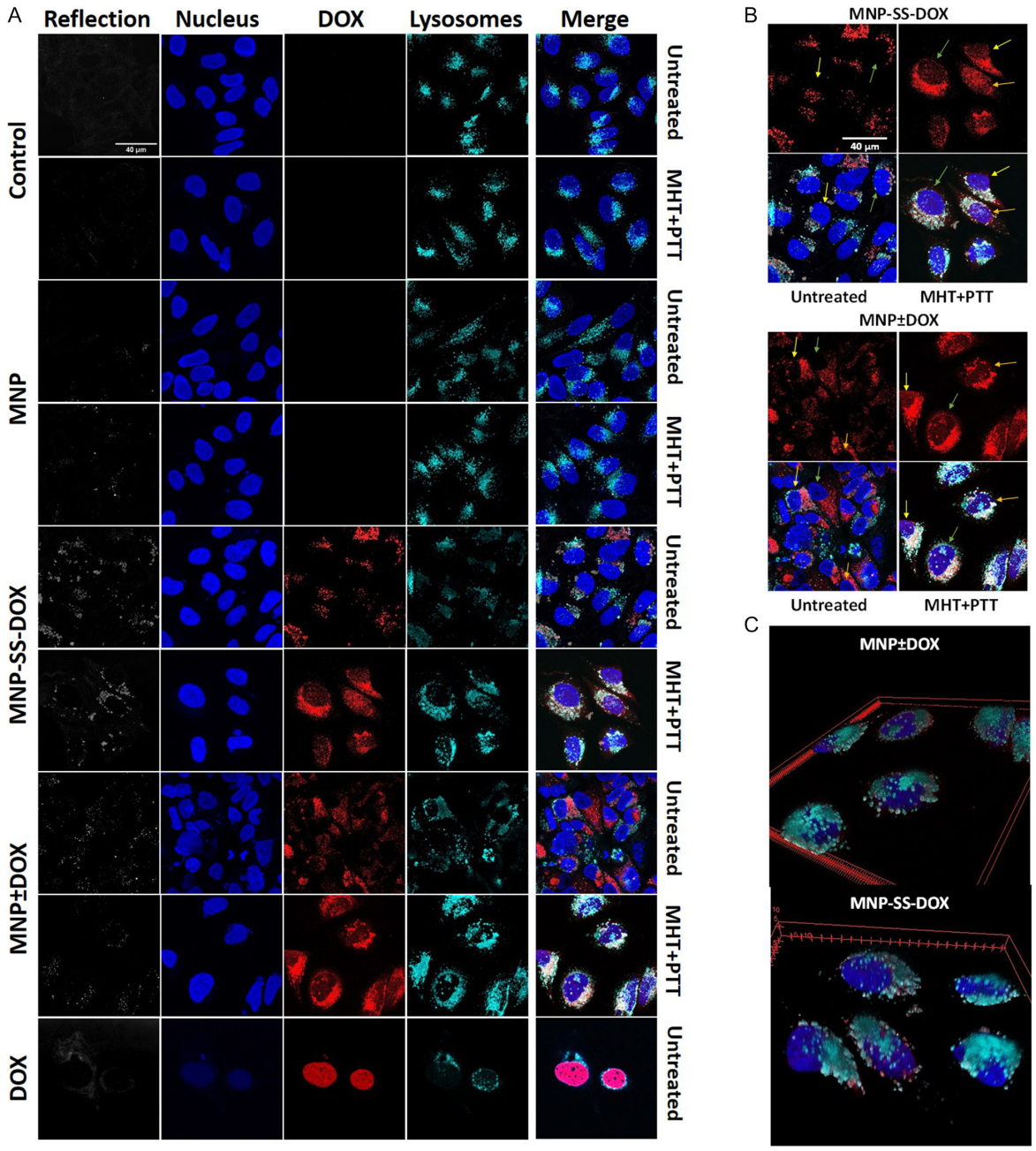

Figure 8. Fluorescence images obtained by confocal microscopy after trimodal chemo-magneto-photothermal treatment. A) Images of each condition showing the reflection in white, the nucleus in blue, DOX in red, and lysosomes in cyan. The last image on the right is the merge of all fluorescence channels. All images are scaled the same as the reflection control image (40 µm). B) Display of the DOX channel only and the merged images showing DOX occupancy in the nucleus after treatment. The colored arrows indicate the pairs in the merged image. In the merged images of the treated cells, more purple nuclei were observed. All images are scaled the same as the first image (40 µm). C) 3D volumetric analysis of MNP-SS-DOX and MNP ± DOX images after thermal treatment, showing that lysosomes are not in the nucleus but rather on top of it.

nucleus, aligning with findings of previous studies on nanoparticle-mediated drug delivery release.

The trimodal chemo-magneto-photothermal treatment effectively integrated localized thermal effects with pH-responsive drug release, significantly reducing tumor cell viability compared to free DOX, and with reduced side effects on healthy cells. To the best of our knowledge, no other *in vitro* studies have comprehensively examined the synergistic application of these three therapeutic modalities. An *in vivo* study demonstrated reduced tumor volumes with trimodal treatment compared to other combinations or free DOX, albeit with high PTT laser power density (5 W cm^{-2}).[51] In contrast, our approach achieves comparable

reductions in tumor viability with significantly lower toxicity and reduced experimental parameters for stimuli induction, potentially minimizing side effects.

4. Conclusions

This study demonstrates the potential of maghemite MNPs functionalized with DOX as powerful agents for chemo-magneto-photothermal therapy, offering a synergistic strategy to enhance cancer treatment outcomes. The trimodal approach effectively combines thermal therapies with chemotherapy at clinically relevant low doses of the magnetic field and the laser application, resulting in enhanced drug release, significant tumor cell death, and minimal toxicity to healthy cells. The use of pH-sensitive release mechanisms and localized heating further underscores the potential of this system to overcome traditional chemotherapy limitations. These findings mark a significant advancement in the clinical translation of multifunctional nanoparticle systems, paving the way for more effective and accessible cancer therapies.

5. Experimental Section

Chemicals: Iron(III) chloride hexahydrate (97% Aldrich), iron(II) chloride tetrahydrate (≥99%, Sigma–Aldrich), ammonium hydroxide solution (25% in water, Sigma–Aldrich), iron(III) nitrate nonahydrate (≥98%, Sigma–Aldrich), nitric acid (70%, Sigma–Aldrich) meso-2,3-dimercaptosuccinic acid (≈98%, Sigma–Aldrich).

Doxorubicin hydrochloride (DOX HCl, 98.0%, Sigma–Aldrich), N-(3-Dimethylaminopropyl)-N′-ethylcarbodiimide hydrochloride (EDC HCL, BioXtra, Sigma–Aldrich), N-Hydroxysuccinimide (NHS, 98%, Sigma–Aldrich), Cysteamine hydrochloride (≥98%, Sigma–Aldrich), sodium hydroxide (≥98%, Sigma–Aldrich), thiol reactive doxorubicin-SS-Pyridine (SS = disulfide, DOX-SS-Pyr).

Dulbecco's Modified Eagle's Medium (DMEM), streptomycin–penicillin (100×), fetal bovine serum (FBS), L-glutamine (100x), trypsin (10×), phosphate–buffered saline (PBS) and cell culture plasticware were purchased from VWR. Resazurin sodium salt and dimethyl sulfoxide (DMSO) were obtained from Sigma–Aldrich.

Synthesis of MNPs (Maghemite (γ-Fe_2O_3)): 14 nm maghemite nanoparticles were obtained following a modified Massart coprecipitation protocol.[52,53] Briefly, 75 mL of NH_4OH (25%) solution were added at a 0.1 mL s^{-1} rate to 425 mL of an aqueous solution of $FeCl_3{\cdot}6H_2O$ (0.334 M) and $FeCl_2{\cdot}4H_2O$ (0.175 M) under vigorous stirring. After 5 min, the reaction was heated to 90 °C for 3 h to increase the particle size. Then, the particles were washed three times with distilled water (100 mL) and collected with the help of a magnet (magnetic decantation). Subsequently, the sample was subjected to acid treatment, as previously described[55] to oxidize Fe_3O_4 to γ-Fe_2O_3 and provide stability against oxidation.[132] 300 mL of HNO_3 (2 M) was added, and the mixture was stirred for 15 min. After that, the supernatant was removed and 75 mL of $Fe(NO_3)_3{\bullet}9H_2O$ (1 M) and 130 mL of water were added to the particles. The mixture was heated to boiling temperature under continuous magnetic stirring for 30 min, cooled down to room temperature, and, by magnetic decantation, the supernatant was substituted by 300 mL of HNO_3 (2 M) and stirred for 15 min. Finally, the particles were washed three times.

For surface coating with meso-2,3-dimercaptosuccinic acid DMSA a published protocol with slight modifications was followed.[133,134] 10 mg (0.027 moles) of DMSA were added to a suspension of 20 mL of particles (86 mg γ-Fe_2O_3) at pH 3 with gentle stirring. The dispersion was sonicated for 2 h. Finally, DMSA-MNPs were dialyzed in water for 4 days, and the pH was adjusted to 7.

Optical Characterization. UV–Vis-NIR Spectroscopy: The absorbance of MNPs were measured using a Cary 60 UV–Vis Spectrophotometer (Agilent) in the 250–1100 nm spectral range using diluted aqueous solutions in standard cuvettes.

Magnetometry Measurements: Under Quasi-Static Conditions: The quasi-static magnetization characterization of the samples was performed using a superconducting quantum interference device (SQUID, MPMS-3) (Quantum Design, San Diego, USA), in DC mode. A small and compact volume of nanoparticles suspension was dried in cotton and introduced in a gelatin capsule to ensure reliable and accurate measurements.[135] Magnetization hysteresis loops at 300 K and thermal dependance of the magnetization were recorded upon ZFC and field cooling (FC) protocols at 100 Oe (8 kA m^{-1}). Measurements were performed at the Laboratory of Magnetism and Magnetotransport of the ICMM-CSIC, Spain.

Magnetometry Measurements: Under Dynamical Conditions: The AC magnetometry characterization of the magnetic colloids were carried out by commercial SENS AC Hyster inductive magnetometer (AC Hyster Series; Nanotech Solutions, Spain). AC Hyster Series measures magnetization cycles from MNPs dispersed in liquid media at room temperature under AMFs whose frequency ranges from 10 up to 100 kHz and intensities up to 24 kA m^{-1}. The studied NPs were dispersed in Milli-Q water at a concentration of 1 g_{Fe} L^{-1}, and 40 µL were pipetted into the measurement vial. Each AC magnetization measurement consists of three repetitions to obtain an average of the magnetization cycles and the related magnetic parameters (H_C, M_R, AC magnetic hysteresis area, $SAR_{MHT,\ AC}$). Magnetization units were normalized by the magnetic element mass (i.e., iron magnetic elements) and expressed in Am^2 kg_{Fe}^{-1}.

Transmission Electron Microscopy (TEM): TEM images were captured using JEM-1400 Flash JEOL operated at 120 kV at the transmission electron microscopy service of CBM-CSIC, Spain. Aqueous dispersion samples were fixed on 400 square-pattern mesh Cu grids with a carbon coating by depositing a drop of solution and letting it dry. The mean nanoparticle core size and its standard deviation (SD) were calculated by measuring >250 nanoparticles from TEM micrographs using ImageJ software.[136] Cell samples underwent washing and fixation with a suspension of 4% PFA and 2% glutaraldehyde in 0.1 mol L^{-1} sodium cacodylate buffer (pH 7.4) for 2 h. Then, they were gradually dehydrated in ethanol (30–100%) and stained with 1% osmium tetroxide containing 1.5% potassium cyanoferrate. The samples were embedded in epoxy resin, cut with a microtome into sections, and mounted on grids for analysis.

X-ray diffraction (XRD): XRD patterns were obtained from lyophilized powder samples using a Bruker D8 Advance A25 system equipped with a PSD Lynseye XE detector. Measurements were performed with Cu Kα radiation over a 2θ range of 10°–80°, using a scan step of 0.02° and positive discrimination.

Elemental Analysis (ICP-OES): Iron concentration of samples was analyzed by ICP-OES using a PerkinElmer Optima 2100 DV equipment. Aqueous dispersion and cell samples were prepared by adding 1 mL of aqua regia (a mixture of HNO_3-HCl in a ratio 1:3) and subjected to 80 °C for 2 h. The sample was then diluted with ultrapure water to a final volume of 10 mL. Isotopic standard reference dilutions of Fe and Au were used to perform a quantification analysis of the elements. Quantitative analysis of the elements was conducted at the Chemical Analysis Service at the ICMM-CSIC, Spain.

Raman Spectroscopy: The vibrational spectra were acquired using a confocal Raman microscope integrated with an atomic force microscope Alpha300 RA Microscope (WITEC, Ulm, Germany) at the vibrational and electronic spectroscopy laboratory (ICV-CSIC, Spain). The microscope was equipped with a Nd:YAG linearly p-polarized laser at 532 nm excitation and was focused by an objective with a numerical aperture of 0.95. The incident laser power was fixed at 0.01–0.02 mW to prevent oxidation changes of the samples. Raman spectra were acquired in the spectral range 0–3600 cm^{-1} using a 600 g mm^{-1} grating. For preparing the samples, a few drops of MNPs dispersions were placed onto a silica buffer and dried for 10 min. 30 single spectra with an integration time of 10 s were accumulated and averaged. The collected spectra were then analyzed with WITec Project Plus software, and Raman mode positions were fitted using Lorentzian functions.

Dynamic Light Scattering (DLS): The hydrodynamic diameter and ζ-potential of the samples were evaluated in a Zetasizer Nano ZS device

(Malvern Panalytical Instruments) using a laser at 633 nm and an angle of 173° between the detector and the sample. Dilute aqueous suspensions of the NPs at a concentration between 0.05 and 0.1 mg mL^{-1} were prepared in a disposable sizing cuvette or in a ζ-potential cell, respectively.

Functionalization of MNPs with Doxorubicin (DOX): Two different strategies were employed to functionalize the MNP with doxorubicin (DOX): through electrostatic interactions (MNP ± DOX) and via disulfide covalent bonding (MNP-SS-DOX).[137]

Functionalization of MNPs with DOX via Electrostatic Interaction (MNP ± DOX): For this, 200 µL of DOX HCl in water (500 µM) were added to 1 mL of MNP-DMSA (2 mg_{Fe} mL^{-1}). The mixture was vortexed and left shaking on a tube rotator overnight, protected from light. The NPs were then centrifuged at 13 200 rpm for 1 h, and the pellet was resuspended in 1 mL of water, sonicated, and washed twice more by centrifugation. The supernatant was measured in the plate reader at 495 nm to obtain the concentration of loaded DOX.

Functionalization of MNPs with DOX via Covalent Bonding (MNP-SS-DOX): A published protocol with slight modifications was followed.[138] To activate the DMSA acids, 20 µL of EDC HCl (120 mM) and 20 µL of NHS (60 mM) were added to 1 mL of DMSA-MNP (2 mg_{Fe} mL^{-1}), and vortexed. They were left shaking overnight. MNPs were washed by centrifugation and redispersed in water. Then, to generate thiol groups (—SH), a mixture of 20 µL of cysteamine HCl (40 mM) and 20 µL of NaOH (40 mM) was added, vortexed, and left shaking overnight. MNPs were washed again and redispersed in water. Finally, 200 µL of DOX-S-S-Pyr dissolved in 500 µM of DMF was added, vortexed, and left shaking overnight. After a centrifugation cycle, the sample was redispersed in 1 mL of water. To calculate the bound doxorubicin, the absorption of 2-pyridinethione in the supernatant was measured using a plate reader at 343 nm.

Drug Release Studies of DOX-Loaded MNPs in Solution: Time-Dependent Drug Release at Varying pH: The release of DOX from MNP-DOX at 2 mg_{Fe} mL^{-1} was carried out by incubating the NPs in PBS at 37 °C (700 µL), with two different concentrations (1 µM and 10 mM) of the reducing agent 1,4-dithiothreitol (DTT, Sigma–Aldrich). The concentration of 1 µM was employed to mimic the extracellular conditions in healthy tissues, whereas the concentration of 10 mM mimicked the intracellular environment in cancerous cells. 100 µL of the initial volume were collected each time to perform the measurement at 30 min, 1, 2, 4, 8 and 24 h. The amount of DOX released was determined by measuring the absorbance at 495 nm of the supernatant of MNP-DOX solution (100 µL; centrifuged 13 200 rpm, 15 min) in a Synergy H4 microplate reader (Agilent BioTek).

Drug Release Studies of DOX-Loaded MNPs in Solution: Drug Release Triggered by MHT, PTT and the Combination of Both, Magneto-Photothermia: The release of DOX triggered by the heat generated by the different thermal treatments was also conducted by incubating 100 µL of the NPs in PBS at 37 °C at two different concentrations of the reducing agent DTT (1 µM and 10 mM). Then, samples were subjected to each treatment as explained in the magneto-photothermal measurements section. Finally, NPs were centrifugated at 13 200 rpm for 15 min and the absorbance of the supernatant was measured at 495 nm in a plate reader in a 96-well plate.

Magneto-Photothermal Measurements. Evaluation of the Heating Efficiency of Nanomaterials in Solution. SAR Values: All studies in solution or in cell pellets involving the use of MHT, PTT, or the combination of both (MHT + PTT, magneto-photothermia) were performed by placing 50–150 µL of the sample in a 500 µL Eppendorf tube.

For photothermia, samples were placed at 15.5 cm from the 808 nm laser source (4 W maximum power, BWT, China) and then subjected to a power laser of 0.15 W during 15 min. MHT were conducted under an AMF of 103 kHz and 20 mT (Magnetherm system, Nanotherics, UK) for 30 min. Prior to the measurements, the interior of the coil was thermalized, and the samples were allowed to stabilize. Magneto-photothermal measurements were performed by subjecting the samples to an AMF of 103 kHz and 20 mT for 30 min, but after the first 15 min, the laser was turned on at 0.15 W, and subsequent 15 min samples were subjected simultaneously to MHT and PTT. All magneto-photothermal experiments were monitored with an infrared thermal camera (FLIR, USA). Next, the treated cells were reseeded into 24-well plates at two different densities (50 000 and 90 000 cells per well) and in duplicate. Finally, viability tests were performed at 24, 48 and 72 h after treatment as described in the next section.

SAR was determined experimentally from the initial linear slope ($t = 30$ s) slope of the temperature curve by the equation:

$$\mathrm{SAR} = \frac{C_w \cdot m_w}{m_{Fe}} \cdot \frac{dT}{dt} \quad (1)$$

Since the mass of the heating element and its heat capacity ($C_{Fe} = 0.449$ J g^{-1} K^{-1}) were significantly lower than those of water or cell solution ($C_w = 4.18$ J g^{-1} K^{-1}, $C_{cell} = 4.125$ J g^{-1} K^{-1}).

X-ray absorption spectroscopy (XAS): XAS experiments were carried out on NPs or on a pool of cells at the Fe K-edge (7112 eV) at the BM23 beamline of the European Synchrotron Radiation Facility (ESRF, Grenoble, France). Measurements were performed both in XANES andEXAFS regimes. XAS spectra of samples were collected in fluorescence mode at room temperature and atmospheric pressure, averaging with several acquisitions. The energy calibration was performed with a metal Fe foil standard. Maghemite and magnetite references were measured in transmission mode. Energy calibration and XAS analysis were performed using the Demeter software package (Athena and Arthemis softwares).[139]

Cell Culture Protocols: Cell Lines and Standard Cell Culture Maintenance: MCF-7 breast adenocarcinoma cells were cultured in DMEM supplemented with 1% L-glutamine, 10% FBS, and 1% streptomycin–penicillin at 37 °C in an incubator with 5% CO_2. The medium was refreshed every 2–3 days. The cells were cultured in a supplemented DMEM medium for 24 h with varying concentrations of nanoparticle suspensions in T75 flasks when they reached high confluence. The concentration of Fe in the extracellular medium was [Fe] = 0.04–0.1 g L^{-1}. Following nanoparticle incubation, the cells were washed and detached by trypsinization when needed.

Cell Culture Protocols: Cell Viability Studies by Alamar Blue Assay: Cell viability was assessed by a colorimetric method based on a resazurin solution assay. A 10% resazurin solution was added to the DMEM medium without red phenol and incubated for 3 h, then transferred to a 96-well plate. Fluorescence was analyzed by a microplate reader (excitation 570 nm, emission 590 nm, Bio-Tek instruments, Inc). Viability was normalized with unlabeled control cells. For the toxicity studies, the Alamar Blue assay was performed right after 24 h of incubation with the nanoparticles or DOX. For the hyperthermia treatments, the analyzes were conducted at 24, 48 and 72 h after the treatment.

Cell Culture Protocols: Prussian Blue Staining: The internalization of iron oxide-based NPs was evaluated using Prussian blue staining. 20 000–40 000 cells were seeded on coverslips in 24-well plates and incubated with NPs for 24 h. Cells were fixed in 4% PFA for 10 min at room temperature. Then, cells were washed and stained with a solution containing equal volume of 4% HCl (Sigma Aldrich) and 4% potassium ferrocyanide trihydrate (Sigma Aldrich) for 20 min. Next, cells were washed with distilled water and then incubated with a solution of 0.5% Neutral Red (Sigma Aldrich) for 5 min. Once the preparations were dried, they were mounted in a coverslip with DPX (VWR) and visualized in a Leica DMI300 B optical microscope with a CCD camera (LEICA DFC310 FX).

Apoptosis/Necrosis Assays with Annexin V/PI Staining Using Flow Cytometry: Cells were reseeded in P100 dishes and 48 h posttreatment the supernatant and cells were collected. Then, samples were washed by centrifugation and one million cells were resuspended in annexin binding buffer 1× (Thermofisher). 10 µL FITC-annexin V 1× were added and incubated for 15 min at 4 °C in the darkness. Then, 380 µL of the binding buffer 1× and 10 µL of propidium iodide 1 mg mL^{-1} were added and the samples were measured in a Beckman Colter Cytomics 500 Flow Cytometer at CNB-CSIC, Spain. Unstained cells and single stained controls of cells treated with DMSO 10% were employed to assign the corresponding gates.

Colocalization of MNPs and DOX. Immunostaining, Alexa 647 and Hoechst – Confocal Microscopy: 24 000 cells per well were seeded in µ-Slide 8-well plates (Ibidi, Germany) after the combination of the chemo-magneto-photothermal treatment. The respective untreated

controls, plus DOX-incubated cells at 5 μM, were also seeded. After 48 h, cells were fixed with 4% PFA for 15 min at room temperature. Cells were then washed and blocked with 10% FBS in PBS for 1 h. Next, the primary antibody mouse anti-LAMP-2 (Thermo Fisher Scientific, USA) was added at a dilution of 1:200 in PBS with 10% FBS and incubated overnight at 4 °C. Then, the cells were washed, and the secondary antibody antimouse-Alexa 647 (Thermo Fisher Scientific, USA) was added diluted 1:500 in PBS with 10% FBS. After 1 h of incubation at room temperature, the antibodies were fixed with 1% PFA. Finally, the nuclei were stained with Hoechst (2 μg mL^{-1}) and the samples were observed under a confocal microscope at the CNB-CSIC, Spain.

Statistical Analysis: All quantitative data were presented as the mean ± SD. The sample size was expressed as *n*. Statistical analysis was performed using Origin and Excel softwares.

Supporting Information

Supporting Information is available from the Wiley Online Library or from the author.

Acknowledgements

This work was funded by MCIN/AEI/10.13039/501100011033 (PID2021-127033OB-C21, PID2020-119352RB-I00, PID2020-117080RB-C53, PID2023-146982OB-I00, PID2023-152944OB-I00, PID2024-161273OB-C21), MCIN/AEI/10.13039/501100011033 and the "European Union NextGenerationEU/PRTR" (CNS2023-144689), CSIC (PIE-20226AT024 and Ayudas Incorporación de Científicos Titulares OEP (ref. 2024ICT15)) and Comunidad de Madrid (2018-T1/IND-1005, ASAP-CM S2022/BMD-7434, S2022/BMD-7403 RENIM-CM and TEC-2024/TEC-380 "Mag4TIC"). IMDEA Nanociencia acknowledges support from the Severo Ochoa program for Centers of Excellence in R&D (CEX2020-001039-S) and FPI grant PRE2020-96246 (R.L.-M.). N.L.-G. also thanks the Spanish Science Ministry (FPU18/02323) for the funding. A.S. acknowledges financial support from grant RYC2021–031236-I funded by MCIN/AEI/10.13039/501100011033 and by the "European Union NextGenerationEU/PRTR". M.P.O. acknowledges the financial support from MICINN for an FPU (FPU20/03166). This work has been funded with 1.026€ million by the Comunidad de Madrid through the LUNABRAIN-CM R&D activities program (TEC-2024/TEC-43), granted by Order 5696/2024. This work was supported by the Severo Ochoa Program for Centers of Excellence in R&D (CEX2024-001445-S), granted to the Instituto de Ciencia de Materiales de Madrid (ICMM-CSIC). The authors are grateful to Milagros Guerra for TEM sample preparation at the Electron Microscopy Service of the Centro de Biología Molecular Severo Ochoa (CBMSO, CSIC-UAM, Spain) and to the technical staff at the Advanced Optical Microscopy facility at CNB-CSIC (Spain), especially to Ana Oña and Jaime Fernández de Córdoba. The authors also acknowledge the support of the technical team at ICMM-CSIC for ICP-OES measurements and the Flow Cytometry Unit at CNB-CSIC (Spain). The authors thank Esteban Urones from the Centro Nacional de Microscopía Electrónica (CNME, Spain) for the acquisition of STEM-EDXS images. Furthermore, the authors acknowledge the BM23 beamline staff at ESRF Synchrotron (Grenoble, France) for their assistance during the experiments. Finally, the authors express their gratitude to the Conexión Nanomedicina network from CSIC.

Conflict of Interest

The authors declare no conflict of interest.

Author Contributions

Rosalía López-Méndez: data curation (equal); formal analysis (equal); investigation (equal); methodology (equal); validation (equal); writing—original draft (equal). **Nuria Lafuente-Gómez**: data curation (equal); formal analysis (equal); investigation (equal); methodology (equal). **Eva Céspedes**: data curation (supporting); formal analysis (supporting); investigation (supporting); methodology (equal). **Mónica Dhanjani**: investigation (supporting); methodology (supporting). **Marina París-Ogáyar**: methodology (supporting). **Francisco José Terán**: methodology (equal); validation (supporting); writing—review and editing (supporting). **Aida Serrano**: data curation (equal); formal analysis (equal); methodology (supporting); writing—review and editing (supporting). **Julio Camarero**: conceptualization (supporting); funding acquisition (supporting); investigation (supporting). **Gorka Salas**: data curation (supporting); investigation (supporting); methodology (equal); writing—review and editing (equal). **Claire Wilhelm**: conceptualization (equal); investigation (equal); methodology (equal); validation (supporting); writing—review and editing (supporting). **Álvaro Somoza**: investigation (equal); methodology (equal); validation (equal); writing—review and editing (equal). **Ana Espinosa**: conceptualization (lead); formal analysis (lead); funding acquisition (lead); investigation (lead); methodology (lead); supervision (lead); writing—original draft (lead).

Keywords

drug delivery, magnetic hyperthermia, nanomedicine, photothermia, X-ray absorption spectroscopy, magneto-photothermia, doxorubicin, chemo-magneto-photo-thermal

Received: April 7, 2025
Revised: August 4, 2025
Published online: September 17, 2025

[1] M. Saeed, W. Ren, A. Wu, *Biomater. Sci.* **2018**, *6*, 708.
[2] R. Weissleder, D. D. Stark, B. L. Engelstad, B. R. Bacon, C. C. Compton, D. L. White, P. Jacobs, J. Lewis, *Am. J. Roentgenol.* **1989**, *152*, 167.
[3] E. A. Perigo, G. Hemery, O. Sandre, D. Ortega, E. Garaio, F. Plazaola, F. J. Teran, *Appl. Phys. Rev.* **2015**, *2*, 041302.
[4] A. Espinosa, J. Reguera, A. Curcio, Á. Muñoz-Noval, C. Kuttner, A. Van de Walle, L. M. Liz-Marzán, C. Wilhelm, *Small* **2020**, *16*, 1904960.
[5] D. D. Stueber, J. Villanova, I. Aponte, Z. Xiao, V. L. Colvin, *Pharmaceutics* **2021**, *13*, 943.
[6] J. W. Bulte, *Adv. Drug Delivery Rev.* **2019**, *138*, 293.
[7] B. T. Mai, P. B. Balakrishnan, M. J. Barthel, F. Piccardi, D. Niculaes, F. Marinaro, S. Fernandes, A. Curcio, H. Kakwere, G. Autret, *ACS Appl. Mater. Interfaces* **2019**, *11*, 5727.
[8] A. C. Silva, T. R. Oliveira, J. B. Mamani, S. M. Malheiros, L. Malavolta, L. F. Pavon, T. T. Sibov, E. Amaro, A. Tannús, E. L. Vidoto, *Int. J. Nanomed.* **2011**, 591.
[9] Z. Hedayatnasab, A. Dabbagh, F. Abnisa, W. M. A. W. Daud, *Eur. Polym. J.* **2020**, *133*, 109789.
[10] M. Chang, Z. Hou, M. Wang, C. Li, J. Lin, *Adv. Mater.* **2021**, *33*, 2004788.
[11] X. Liu, Y. Zhang, Y. Wang, W. Zhu, G. Li, X. Ma, Y. Zhang, S. Chen, S. Tiwari, K. Shi, *Theranostics* **2020**, *10*, 3793.
[12] Z. V. Díaz-Riascos, M. Llaguno-Munive, N. Lafuente-Gómez, Y. Luengo, S. Holmes, J. Volatron, O. Ibarrola, S. Mancilla, F. Sarno, J. J. Aguirre, *ACS Appl. Mater. Interfaces* **2025**, *17*, 2924.
[13] C. Sanson, O. Diou, J. Thevenot, E. Ibarboure, A. Soum, A. Brûlet, S. Miraux, E. Thiaudière, S. Tan, A. Brisson, *ACS Nano* **2011**, *5*, 1122.
[14] A. Espinosa, R. Di Corato, J. Kolosnjaj-Tabi, P. Flaud, T. Pellegrino, C. Wilhelm, *ACS Nano* **2016**, *10*, 2436.

[15] H. Chen, J. Burnett, F. Zhang, J. Zhang, H. Paholak, D. Sun, *J. Mater. Chem. B* **2014**, *2*, 757.
[16] Z. Zhou, Y. Sun, J. Shen, J. Wei, C. Yu, B. Kong, W. Liu, H. Yang, S. Yang, W. Wang, *Biomaterials* **2014**, *35*, 7470.
[17] Q.-F. Meng, L. Rao, M. Zan, M. Chen, G.-T. Yu, X. Wei, Z. Wu, Y. Sun, S.-S. Guo, X.-Z. Zhao, *Nanotechnology* **2018**, *29*, 134004.
[18] A. Espinosa, J. Kolosnjaj-Tabi, A. Abou-Hassan, A. Plan Sangnier, A. Curcio, A. K. Silva, R. Di Corato, S. Neveu, T. Pellegrino, L. M. Liz-Marzán, *Adv. Funct. Mater.* **2018**, *28*, 1803660.
[19] S. Cabana, A. Curcio, A. Michel, C. Wilhelm, A. Abou-Hassan, *Nanomaterials* **2020**, *10*, 1548.
[20] E. Bertuit, E. Benassai, G. Mériguet, J.-M. Greneche, B. Baptiste, S. Neveu, C. Wilhelm, A. Abou-Hassan, *ACS Nano* **2021**, *16*, 271.
[21] C. Lozano-Pedraza, E. Plaza-Mayoral, A. Espinosa, B. Sot, A. Serrano, G. Salas, C. Blanco-Andujar, G. Cotin, D. Felder-Flesch, S. Begin-Colin, *Nanoscale Adv.* **2021**, *3*, 6490.
[22] S. Zhao, X. Yu, Y. Qian, W. Chen, J. Shen, *Theranostics* **2020**, *10*, 6278.
[23] S. Shen, S. Wang, R. Zheng, X. Zhu, X. Jiang, D. Fu, W. Yang, *Biomaterials* **2015**, *39*, 67.
[24] M. Chu, Y. Shao, J. Peng, X. Dai, H. Li, Q. Wu, D. Shi, *Biomaterials* **2013**, *34*, 4078.
[25] X. Ren, R. Zheng, X. Fang, X. Wang, X. Zhang, W. Yang, X. Sha, *Biomaterials* **2016**, *92*, 13.
[26] L. Rao, B. Cai, L.-L. Bu, Q.-Q. Liao, S.-S. Guo, X.-Z. Zhao, W.-F. Dong, W. Liu, *ACS Nano* **2017**, *11*, 3496.
[27] H. Rodríguez-Rodríguez, G. Salas, J. R. Arias-Gonzalez, *J. Phys. Chem. Lett.* **2020**, *11*, 2182.
[28] S. Nemec, S. Kralj, C. Wilhelm, A. Abou-Hassan, M.-P. Rols, J. Kolosnjaj-Tabi, *Applied Sciences* **2020**, *10*, 7322.
[29] J. Estelrich, M. A. Busquets, *Molecules* **2018**, *23*, 1567.
[30] C. de la Encarnación, D. J. de Aberasturi, L. M. Liz-Marzán, *Adv. Drug Delivery Rev.* **2022**, *189*, 114484.
[31] A. Espinosa, M. Bugnet, G. Radtke, S. Neveu, G. A. Botton, C. Wilhelm, A. Abou-Hassan, *Nanoscale* **2015**, *7*, 18872.
[32] E. Cazares-Cortes, C. Wilhelm, J. E. Perez, A. Espinosa, S. Casale, A. Michel, A. Abou-Hassan, C. Ménager, *Chem. Commun.* **2021**, *57*, 5945.
[33] A. Espinosa, J. Reguera, A. Curcio, Á. Muñoz-Noval, C. Kuttner, A. Van de Walle, L. M. Liz-Marzán, C. Wilhelm, *Small* **2020**, *16*, 1904960.
[34] E. S. Abu Serea, I. A. Orue, J. A. García, S. Lanceros-Méndez, J. Reguera, *ACS Appl. Nano Mater.* **2023**, *6*, 18466.
[35] A. Figuerola, A. Espinosa, A. Abou-Hassan, M. Estrader, C. Whilelm, *Mater. Horiz.* **2023**, *10*, 4757.
[36] T. Vangijzegem, D. Stanicki, S. Laurent, *Expert Opin. Drug Delivery* **2019**, *16*, 69.
[37] C. A. Quinto, P. Mohindra, S. Tong, G. Bao, *Nanoscale* **2015**, *7*, 12728.
[38] C. Wang, H. Xu, C. Liang, Y. Liu, Z. Li, G. Yang, L. Cheng, Y. Li, Z. Liu, *ACS Nano* **2013**, *7*, 6782.
[39] T. T. N'Guyen, H. T. Duong, J. Basuki, V. Montembault, S. Pascual, C. Guibert, J. Fresnais, C. Boyer, M. R. Whittaker, T. P. Davis, *Angew. Chem.* **2013**, *125*, 14402.
[40] F. Benyettou, J. A. Ocadiz Flores, F. Ravaux, R. Rezgui, M. Jouiad, S. I. Nehme, R. K. Parsapur, J. C. Olsen, P. Selvam, A. Trabolsi, *Chem. – Eur. J.* **2016**, *22*, 17020.
[41] S. Kossatz, J. Grandke, P. Couleaud, A. Latorre, A. Aires, K. Crosbie-Staunton, R. Ludwig, H. Dähring, V. Ettelt, A. Lazaro-Carrillo, *Breast Cancer Res.* **2015**, *17*, 66.
[42] E. Cazares-Cortes, A. Espinosa, J.-M. Guigner, A. Michel, N. Griffete, C. Wilhelm, C. Ménager, *ACS Appl. Mater. Interfaces* **2017**, *9*, 25775.
[43] N. Lafuente-Gómez, P. Milán-Rois, D. García-Soriano, Y. Luengo, M. Cordani, H. Alarcón-Iniesta, G. Salas, Á. Somoza, *Cancers* **2021**, *13*, 4095.
[44] Z. Ferjaoui, E. Jamal Al Dine, A. Kulmukhamedova, L. Bezdetnaya, C. Soon Chang, R. Schneider, F. Mutelet, D. Mertz, S. Begin-Colin, F. Quilès, *ACS Appl. Mater. Interfaces* **2019**, *11*, 30610.
[45] Y. M. Kwon, J. Y. Je, S. H. Cha, Y. Oh, W. H. Cho, *Oncol. Rep.* **2019**, *42*, 1709.
[46] X. Guo, W. Li, L. Luo, Z. Wang, Q. Li, F. Kong, H. Zhang, J. Yang, C. Zhu, Y. Du, *ACS Appl. Mater. Interfaces* **2017**, *9*, 16581.
[47] X. Ma, H. Tao, K. Yang, L. Feng, L. Cheng, X. Shi, Y. Li, L. Guo, Z. Liu, *Nano Res.* **2012**, *5*, 199.
[48] L. Sun, Q. Li, L. Zhang, Z. Xu, Y. Kang, P. Xue, *ACS Appl. Nano Mater.* **2017**, *1*, 325.
[49] Y. Jabalera, A. Sola-Leyva, S. C. Gaglio, M. P. Carrasco-Jiménez, G. R. Iglesias, M. Perduca, C. Jimenez-Lopez, *Pharmaceutics* **2021**, *13*, 1168.
[50] S. Balasubramanian, A. R. Girija, Y. Nagaoka, T. Fukuda, S. Iwai, V. Kizhikkilot, K. Kato, T. Maekawa, S. D. Nair, *RSC Adv.* **2015**, *5*, 25066.
[51] M. Sharifi, A. Hasan, N. M. Q. Nanakali, A. Salihi, F. A. Qadir, H. A. Muhammad, M. S. Shekha, F. M. Aziz, K. M. Amen, F. Najafi, *Sci. Rep.* **2020**, *10*, 5925.
[52] R. Massart, *IEEE Trans. Magn.* **1981**, *17*, 1247.
[53] Y. Luengo, Z. V. Díaz-Riascos, D. García-Soriano, F. J. Teran, E. J. Artés-Ibáñez, O. Ibarrola, Á. Somoza, R. Miranda, S. Schwartz, I. Abasolo, *Pharmaceutics* **2022**, *14*, 1526.
[54] A. Bee, R. Massart, S. Neveu, *J. Magn. Magn. Mater.* **1995**, *149*, 6.
[55] R. Costo, V. Bello, C. Robic, M. Port, J. F. Marco, M. Puerto Morales, S. Veintemillas-Verdaguer, *Langmuir* **2012**, *28*, 178.
[56] B. S. Yadav, R. Singh, A. K. Vishwakarma, N. Kumar, *J. Supercond. Novel Magn.* **2020**, *33*, 2199.
[57] V. F. Cardoso, A. Francesko, C. Ribeiro, M. Bañobre-López, P. Martins, S. Lanceros-Mendez, *Adv. Healthcare Mater.* **2018**, *7*, 1700845.
[58] M. A. Legodi, D. de Waal, *Dyes Pigm.* **2007**, *74*, 161.
[59] T. Daou, G. Pourroy, S. Bégin-Colin, J.-M. Greneche, C. Ulhaq-Bouillet, P. Legaré, P. Bernhardt, C. Leuvrey, G. Rogez, *Chem. Mater.* **2006**, *18*, 4399.
[60] M. M. Can, S. Ozcan, A. Ceylan, T. Firat, *Mater. Sci. Eng., B* **2010**, *172*, 72.
[61] A. Serrano, O. Rodríguez de La Fuente, M. García-Hernández, G. Campo, C. de Julián Fernández, J. Fernández, M. García, *Appl Phys Lett* **2018**, *113*, 101908.
[62] M. Kumar, A. Sharma, I. K. Maurya, A. Thakur, S. Kumar, *J. Taibah Univ. Sci.* **2019**, *13*, 280.
[63] S. S. Behera, J. K. Patra, K. Pramanik, N. Panda, H. Thatoi, *World J. Nano Sci. Eng.* **2012**, *2*, 196.
[64] F. Geinguenaud, C. Banissi, A. F. Carpentier, L. Motte, *Nanomaterials* **2015**, *5*, 1588.
[65] N. Rahoui, B. Jiang, N. Taloub, M. Hegazy, Y. D. Huang, *J. Biomater. Sci., Polym. Ed.* **2018**, *29*, 1482.
[66] C. Coluccini, Y. M. Ng, Y. I. A. Reyes, H.-Y. T. Chen, Y. L. Khung, *Molecules* **2020**, *25*, 5455.
[67] N. Singh, F. Sallem, C. Mirjolet, T. Nury, S. K. Sahoo, N. Millot, R. Kumar, *Nanomaterials* **2019**, *9*, 138.
[68] I. I. Lungu, S. Nistorescu, M. A. Badea, A.-M. Petre, A.-M. Udrea, A.-M. Banici, C. Fleacă, E. Andronescu, A. Dinischiotu, F. Dumitrache, *Polymers* **2020**, *12*, 2799.
[69] S.-M. Zhou, D.-K. Ma, S.-H. Zhang, W. Wang, W. Chen, S.-M. Huang, K. Yu, *Nanoscale* **2016**, *8*, 1374.
[70] A. Loren, C. Eliasson, M. Josefson, K. Murty, M. Käll, J. Abrahamsson, K. Abrahamsson, *J. Raman Spectrosc.* **2001**, *32*, 971.
[71] C. Eliasson, A. Lorén, K. Murty, M. Josefson, M. Käll, J. Abrahamsson, K. Abrahamsson, *Spectrochim. Acta, Part A* **2001**, *57*, 1907.
[72] Z. Farhane, F. Bonnier, A. Casey, H. J. Byrne, *Analyst* **2015**, *140*, 4212.

[73] M. I. Majeed, Q. Lu, W. Yan, Z. Li, I. Hussain, M. N. Tahir, W. Tremel, B. Tan, *J. Mater. Chem. B* **2013**, *1*, 2874.
[74] N. Mallick, M. Anwar, M. Asfer, S. H. Mehdi, M. M. A. Rizvi, A. K. Panda, S. Talegaonkar, F. J. Ahmad, *Carbohydr. Polym.* **2016**, *151*, 546.
[75] Y. Oh, M. S. Moorthy, P. Manivasagan, S. Bharathiraja, J. Oh, *Biochimie* **2017**, *133*, 7.
[76] T. Nizamov, A. Garanina, I. Grebennikov, O. Zhironkina, O. Strelkova, I. Alieva, I. Kireev, M. Abakumov, A. Savchenko, A. Majouga, *BioNanoScience* **2018**, *8*, 394.
[77] E. P. Hernandes, D. Lazarin-Bidóia, R. D. Bini, C. V. Nakamura, L. F. Cótica, S. de Oliveira Silva Lautenschlager, *Antioxidants* **2023**, *12*, 237.
[78] S. P. Schwaminger, P. Fraga-García, F. Selbach, F. G. Hein, E. C. Fuß, R. Surya, H.-C. Roth, S. A. Blank-Shim, F. E. Wagner, S. Heissler, *Adsorption* **2017**, *23*, 281.
[79] S. Schwaminger, D. Bauer, P. Fraga-García, F. Wagner, S. Berensmeier, *CrystEngComm* **2017**, *19*, 246.
[80] J. Sifford, K. J. Walsh, S. Tong, G. Bao, G. Agarwal, *Nanoscale Adv.* **2019**, *1*, 2348.
[81] N. V. Mdlovu, K.-S. Lin, Y. Chen, R.-S. Juang, T.-W. Chang, N. B. Mdlovu, *J. Taiwan Inst. Chem. Eng.* **2019**, *104*, 260.
[82] G. Lawes, R. Naik, P. Vaishnavab, *NanoCellBiology* **2014**, 257.
[83] J. Reguera, D. J. de Aberasturi, M. Henriksen-Lacey, J. Langer, A. Espinosa, B. Szczupak, C. Wilhelm, L. M. Liz-Marzán, *Nanoscale* **2017**, *9*, 9467.
[84] A. Peigneux, F. Oltolina, D. Colangelo, G. R. Iglesias, A. V. Delgado, M. Prat, C. Jimenez-Lopez, *Part. Part. Syst. Charact.* **2019**, *36*, 1900057.
[85] P. Lenox, L. K. Plummer, P. Paul, J. E. Hutchison, A. Jander, P. Dhagat, *IEEE Magn. Lett.* **2017**, *9*, 6500405.
[86] A. S. Eggeman, S. A. Majetich, D. Farrell, Q. A. Pankhurst, *IEEE Trans. Magn.* **2007**, *43*, 2451.
[87] D. Cabrera, A. Coene, J. Leliaert, E. J. Artés-Ibáñez, L. Dupré, N. D. Telling, F. J. Teran, *ACS Nano* **2018**, *12*, 2741.
[88] E. Sanz-de Diego, A. Aires, P. Palacios-Alonso, D. Cabrera, N. Silvestri, C. C. Vequi-Suplicy, E. J. Artés-Ibáñez, J. Requejo-Isidro, R. Delgado-Buscalioni, T. Pellegrino, *Nanoscale* **2024**, *16*, 4082.
[89] M. Lázaro, P. Lupiáñez, J. L. Arias, M. P. Carrasco-Jiménez, Á. V. Delgado, G. R. Iglesias, *Polymers* **2022**, *14*, 4913.
[90] M. E. Fortes Brollo, A. Domínguez-Bajo, A. Tabero, V. Dominguez-Arca, V. Gisbert, G. Prieto, C. Johansson, R. Garcia, A. Villanueva, M. C. Serrano, *ACS Appl. Mater. Interfaces* **2020**, *12*, 4295.
[91] T. Park, R. Amatya, K. A. Min, M. C. Shin, *Pharmaceutics* **2023**, *15*, 292.
[92] X. Fu, X. Wang, S. Zhou, Y. Zhang, *Int. J. Nanomed.* **2017**, *2017*, 3751.
[93] L. Wu, L. Chen, F. Liu, X. Qi, Y. Ge, S. Shen, *Colloids Surf., B* **2017**, *152*, 440.
[94] M. M. Swidan, N. S. Wahba, T. M. Sakr, *Cancer Nanotechnol.* **2024**, *15*, 28.
[95] M. S. Maashi, M. Al-Mualm, G. R. L. Al-Awsi, M. J. C. Opulencia, M. E. Al-Gazally, B. Abdullaev, W. K. Abdelbasset, M. J. Ansari, A. T. Jalil, F. Alsaikhan, *Mol. Biol. Rep.* **2022**, *49*, 8777.
[96] A. Abdullah, S. Abdulkarim, A. Rasedee, S. Mohamed Elwathig, M. Al-Qubaisi, *BMC Complem. Altern. Med.* **2014**, *14*, 199.
[97] S. Ramazi, M. Salimian, A. Allahverdi, S. Kianamiri, P. Abdolmaleki, *Sci. Rep.* **2023**, *13*, 8844.
[98] E. M. Radwan, R. Abdullah, M. S. Al-Qubaisi, M. E. El Zowalaty, S. E. Naadja, N. B. Alitheen, A. R. Omar**2016**, *13*, 3945.
[99] M. Calero, M. Chiappi, A. Lazaro-Carrillo, M. J. Rodríguez, F. J. Chichón, K. Crosbie-Staunton, A. Prina-Mello, Y. Volkov, A. Villanueva, J. L. Carrascosa, *J. Nanobiotechnol.* **2015**, *13*, 16.
[100] M. Kumar, G. Singh, V. Arora, S. Mewar, U. Sharma, N. Jagannathan, S. Sapra, A. K. Dinda, S. Kharbanda, H. Singh, *Int. J. Nanomed.* **2012**, *2012*, 3503.
[101] H.-S. Kim, Y.-S. Lee, D.-K. Kim, *Pharmacology* **2009**, *84*, 300.
[102] O. Bar-On, M. A. Shapira, D. D. Hershko, *Anti-Cancer Drugs* **2007**, *18*, 1113.
[103] D. García-Soriano, P. Milán-Rois, N. Lafuente-Gómez, C. Rodríguez-Díaz, C. Navío, Á. Somoza, G. Salas, *J. Colloid Interface Sci.* **2024**, *670*, 73.
[104] A. Kuzmin, J. Chaboy, *IUCrJ* **2014**, *1*, 571.
[105] I. Milosevic, L. Motte, B. Aoun, T. Li, Y. Ren, C. Sun, M.-L. Saboungi, *Biochim. Biophys. Acta* **2017**, *1861*, 3621.
[106] A. Espinosa, A. Serrano, A. Llavona, J. J. De La Morena, M. Abuin, A. Figuerola, T. Pellegrino, J. Fernández, M. Garcia-Hernandez, G. Castro, *Meas. Sci. Technol.* **2011**, *23*, 015602.
[107] C. Piquer, M. Laguna-Marco, A. G. Roca, R. Boada, C. Guglieri, J. Chaboy, *J. Phys. Chem. C* **2014**, *118*, 1332.
[108] A. Corrias, G. Mountjoy, D. Loche, V. Puntes, A. Falqui, M. Zanella, W. J. Parak, M. F. Casula, *J. Phys. Chem. C* **2009**, *113*, 18667.
[109] R. M. Cornell, U. Schwertmann, *The Iron Oxides: Structure, Properties, Reactions, Occurrences, and Uses*, Vol. *664*, Wiley-VCH, Weinheim **2003**.
[110] A. Espinosa, A. Munoz-Noval, M. García-Hernández, A. Serrano, J. J. de la Morena, A. Figuerola, A. Quarta, T. Pellegrino, C. Wilhelm, M. García, *J. Nanopart. Res.* **2013**, *15*, 1514.
[111] R. Di Corato, A. Espinosa, L. Lartigue, M. Tharaud, S. Chat, T. Pellegrino, C. Ménager, F. Gazeau, C. Wilhelm, *Biomaterials* **2014**, *35*, 6400.
[112] R. López-Méndez, J. Reguera, A. Fromain, E. S. Abu Serea, E. Céspedes, F. Terán, F. Zheng, A. Parente, M. Á. García, E. Fonda, C. Wilhelm, J. Camarero, A. Muñoz-Noval, A. Espinosa, *Adv. Healthcare Mater.* **2023**, *12*, 2301863.
[113] R. Di Corato, G. Béalle, J. Kolosnjaj-Tabi, A. Espinosa, O. Clement, A. K. Silva, C. Menager, C. Wilhelm, *ACS Nano* **2015**, *9*, 2904.
[114] D. Soukup, S. Moise, E. Céspedes, J. Dobson, N. D. Telling, *ACS Nano* **2015**, *9*, 231.
[115] F. Benyettou, H. Fahs, R. Elkharrag, R. A. Bilbeisi, B. Asma, R. Rezgui, L. Motte, M. Magzoub, J. Brandel, J.-C. Olsen, *RSC Adv.* **2017**, *7*, 23827.
[116] F. Serio, N. Silvestri, S. K. Avugadda, G. E. Nucci, S. Nitti, V. Onesto, F. Catalano, E. D'Amone, G. Gigli, L. L. Del Mercato, *J. Colloid Interface Sci.* **2022**, *607*, 34.
[117] Y. Oh, J.-Y. Je, M. S. Moorthy, H. Seo, W. H. Cho, *Int. J. Pharm.* **2017**, *531*, 1.
[118] A. S. Song, A. M. Najjar, K. R. Diller, *J. Biomech. Eng.* **2014**, *136*, 071006.
[119] N. D. Thorat, O. Lemine, R. A. Bohara, K. Omri, L. El Mir, S. A. Tofail, *Phys. Chem. Chem. Phys.* **2016**, *18*, 21331.
[120] B. Ding, S. Shen, L. Wu, X. Qi, H. Ni, Y. Ge, *Chem. Lett.* **2015**, *44*, 858.
[121] Y. Xu, Y. Zhu, S. Kaskel, *RSC Adv.* **2015**, *5*, 99875.
[122] Y. S. Tor, L. S. Yazan, J. B. Foo, N. Armania, Y. K. Cheah, R. Abdullah, M. U. Imam, N. Ismail, M. Ismail, *BMC Complement Altern. Med.* **2014**, *14*, 55.
[123] R. Hergt, S. Dutz, *J. Magn. Magn. Mater.* **2007**, *311*, 187.
[124] A. Ansi, *122: ANSI (American National Standards Institute) American National Standard for Safe Use of Lasers (ANSI Z136.1-2007)*, Laser Institute of America, Orlando, FL **2007**.
[125] M. Soldatov, O. Polozhentsev, P. Zolotukhin, A. Belanova, M. Cotte, H. Castillo-Michel, A. P. del Real, E. Kuchma, A. Soldatov, *Radiat. Phys. Chem.* **2021**, *179*, 109162.
[126] M. L. Fdez-Gubieda, A. Muela, J. Alonso, A. García-Prieto, L. Olivi, R. Fernández-Pacheco, J. M. Barandiarán, *ACS Nano* **2013**, *7*, 3297.

[127] A. Curcio, A. Van de Walle, A. Serrano, S. Preveral, C. Péchoux, D. Pignol, N. Menguy, C. T. Lefevre, A. Espinosa, C. Wilhelm, *ACS Nano* **2020**, *14*, 1406.
[128] L. Gandarias, A. G. Gubieda, G. Gorni, O. Mathon, L. Olivi, A. Abad-Díaz-de-Cerio, M. L. Fdez-Gubieda, A. Muela, A. García-Prieto, *Biotechnol. J.* **2023**, *18*, 2300173.
[129] A. Fromain, A. Van de Walle, G. Curé, C. Péchoux, A. Serrano, Y. Lalatonne, A. Espinosa, C. Wilhelm, *Nanoscale* **2023**, *15*, 10097.
[130] X. Chu, L. Zhang, Y. Li, Y. He, Y. Zhang, C. Du, *Small* **2023**, *19*, 2205414.
[131] Z. Jin, Y. Dun, L. Xie, W. Jiang, X. Sun, P. Hu, S. Zheng, Y. Yu, *Colloids Surf., B* **2021**, *208*, 112107.
[132] M. Safi, J. Courtois, M. Seigneuret, H. Conjeaud, J.-F. Berret, *Biomaterials* **2011**, *32*, 9353.
[133] Y. Luengo, S. Nardecchia, M. P. Morales, M. C. Serrano, *Nanoscale* **2013**, *5*, 11428.
[134] N. Fauconnier, J. Pons, J. Roger, A. Bee, *J. Colloid Interface Sci.* **1997**, *194*, 427.
[135] C. Amorim, F. Mohseni, R. Dumas, V. Amaral, J. Amaral, *Meas. Sci. Technol.* **2021**, *32*, 105602.
[136] C. A. Schneider, W. S. Rasband, K. W. Eliceiri, *Nat. Methods* **2012**, *9*, 671.
[137] A. Latorre, Á. Somoza, *Curr. Top. Med. Chem.* **2014**, *14*, 2662.
[138] A. Latorre, P. Couleaud, A. Aires, A. L. Cortajarena, Á. Somoza, *Eur. J. Med. Chem.* **2014**, *82*, 355.
[139] B. Ravel, M. Newville, *J. Synchrotron Radiat.* **2005**, *12*, 537.